Coordination of Pickpocket ion channel delivery and dendrite growth in Drosophila sensory neurons

Josephine W. Mitchell[1,2], Ipek Midillioglu[3], Bei Wang[4,5], Chun Han[4,5], and Jill Wildonger[2,3,6*]

[1]Integrated Program in Biochemistry, University of Wisconsin-Madison, Madison, WI 53706
[2]Biochemistry Department, University of Wisconsin-Madison, Madison, WI 53706
[3]Pediatrics Department, University of California, San Diego, La Jolla, CA 92093
[4]Weill Institute for Cell and Molecular Biology, Cornell University, Ithaca, NY 14853
[5]Department of Molecular Biology and Genetics, Cornell University, Ithaca, NY 14853
[6]School of Biological Sciences, Cell & Developmental Biology, University of California, San Diego, La Jolla, CA 92093

*Correspondence: jwildonger@ucsd.edu

Abstract

Sensory neurons enable an organism to perceive external stimuli, which is essential for survival. The sensory capacity of a neuron depends on the elaboration of its dendritic arbor and the delivery of sensory ion channels to the dendritic membrane. However, it is not well understood how ion channels are trafficked to sensory dendrites and whether their delivery is coordinated with dendrite growth. We investigated the trafficking of the DEG/ENaC/ASIC ion channel Pickpocket (Ppk) in peripheral sensory neurons in fruit fly larvae. We used CRISPR-Cas9 genome engineering to tag endogenous Ppk1 and visualize it live, including monitoring Ppk1 membrane localization via a novel secreted split-GFP approach. Strikingly, Ppk1 is present throughout the membrane of actively growing dendrites, and Ppk1 density scales in proportion to the dendritic membrane, even when dynein-mediated transport to dendrites is disrupted. Our data suggest that Ppk1 is integral to the membrane of growing dendrites and implicate the recycling endosome GTPase Rab11 in the forward trafficking of Ppk1 to dendrites. Together, our results suggest that Ppk channel transport is coordinated with dendrite morphogenesis, thus ensuring proper ion channel levels and distribution in sensory dendrites.

Introduction

An organism's interactions with its environment rely on its ability to sense external stimuli through sensory neurons. Ion channels distributed throughout the dendritic arbor of a sensory neuron rapidly transduce external stimuli into cellular signals. Both the morphology of a sensory neuron's dendritic arbor and the localization of ion channels in the arbor are essential to the establishment of a neuron's receptive field and sensory capacity. While the localization of ion channels to synapses in the central nervous system has been well studied (Bourke et al., 2018), little is known regarding mechanisms that regulate the delivery of ion channels to the dendritic membrane of sensory neurons in the peripheral nervous system. It is also not known whether and how this trafficking may be coordinated with dendrite morphogenesis to establish the proper distribution of ion channels needed for sensing environmental stimuli.

To investigate the relationship between ion channel trafficking and dendrite growth, we used the *Drosophila melanogaster* class IV dendritic arborization (da) neurons as a model. The class IV da neurons function as polymodal nociceptors that detect multiple stimuli (thermal, mechanical, and light) and extend elaborately branched dendritic arbors that cover the larval body wall (Grueber et al., 2002; Hwang et al., 2007; Tracey et al., 2003; Xiang et al., 2010). These neurons are an ideal model to study ion channel delivery in growing sensory dendrites for several reasons. First, during larval development, the class IV da neuron dendrites undergo expansive growth that can be easily visualized live in intact animals due to their superficial location just beneath the transparent larval cuticle and their relatively flat, two-dimensional morphology (Grueber et al., 2003; Parrish et al., 2009). Second, the class IV da neurons have been a powerful *in vivo* model to identify mechanisms of dendrite morphogenesis, including players involved in membrane production and trafficking, the secretory and endosomal networks, molecular motor-based transport, and the cytoskeleton (Jan and Jan, 2010; Singhania and Grueber, 2014). By manipulating known mechanisms of dendrite arbor growth, we can investigate how ion channel trafficking is coordinated with dendrite morphogenesis. Third, the general morphology and function of the class IV neurons is similar to peripheral sensory neurons and nociceptors in other organisms, including the mammalian C- and Aδ-fibers and the worm PVD and FLP neurons (Hall and Treinin, 2011; He et al., 2022; Lumpkin and Caterina, 2007). Thus, studying ion channel trafficking in the class IV da neurons may shed light on conserved mechanisms of ion channel localization in sensory dendrites.

71 During neuronal morphogenesis, the class IV da neurons express several dendritic ion channels
72 that have been structurally and functionally characterized, including pickpocket (Ppk); Transient
73 Receptor Potential (TRP) channels, such as painless; and Piezo (Adams et al., 1998; Coste et
74 al., 2012; Kim et al., 2012; Tracey et al., 2003; Zhong et al., 2010). Whereas TRP and Piezo
75 channels are comprised of large multi-pass membrane protein subunits, the Ppk ion channel
76 subunits are relatively small, two-pass membrane proteins. Their modest size makes
77 endogenous Ppk channels amenable to manipulation via CRISPR-Cas9 genome engineering.
78 Moreover, the crystal structure of a conserved Ppk ortholog in chickens, ASIC1, has been
79 solved, and this information is advantageous for the structure-guided manipulation of Ppk (Jasti
80 et al., 2007). For these reasons we decided to focus on investigating the trafficking of Ppk in the
81 class IV da neurons.
82
83 Ppk proteins belong to the large, structurally conserved family of Degenerin/Epithelial Na^+
84 Channel/Acid Sensing Ion Channels (DEG/ENaC/ASICs) whose members in worms, flies, fish,
85 and mammals carry out a variety of functions ranging from mechanosensation and learning and
86 memory in the nervous system to salt homeostasis in epithelial cells in the kidney (Bianchi,
87 2022; Boscardin et al., 2016; Kellenberger and Schild, 2002). In the fly class IV da neurons, the
88 Ppk channel is composed of two subunits, Pickpocket 1 (Ppk1) and Pickpocket 26 (Ppk26),
89 which are mutually dependent on each other for membrane expression (Adams et al., 1998;
90 Gorczyca et al., 2014; Guo et al., 2014; Mauthner et al., 2014). The localization of Ppk1 and
91 Ppk26 has been characterized using antibodies and fluorescently tagged transgenes, and both
92 subunits are broadly distributed throughout the developing dendrites of class IV da neurons.
93 Interestingly, Ppk1 and Ppk26 are expressed from late-embryo to mid-larval stages, which
94 coincides with a period of rapid dendrite growth (Adams et al., 1998; Darboux et al., 1998;
95 Gorczyca et al., 2014; Jaszczak et al., 2022; Parrish et al., 2009; Zelle et al., 2013). The timing
96 of Ppk1 and Ppk26 expression suggests that Ppk channel production and localization may be
97 coordinated with dendrite growth.
98
99 To investigate the potential coordination of Ppk1 trafficking and dendrite growth, we used
100 CRISPR-Cas9 genome engineering to tag endogenous Ppk1 and follow its localization in
101 growing dendrites. We found that in developing neurons, Ppk1 is enriched throughout dendrites
102 and is also present in axon terminals and at low levels in axons. Using a new split-GFP strategy
103 to monitor the insertion of proteins into the cell membrane, we visualized Ppk1 membrane
104 expression live in developing neurons, which revealed the robust, uniform membrane

105 localization of Ppk1 in the somatodendritic compartment. We found that Ppk1 was present
106 throughout growing dendrite branches and in actively growing dendrite tips, suggesting that
107 Ppk1 is part of the nascent membrane that is adding to growing dendrites. In support of this
108 model, we found that Ppk1 dendritic levels scale in proportion to the amount of dendritic
109 membrane, even when transport to dendrites is disrupted by perturbing dynein. We also
110 discovered that the recycling endosome GTPase Rab11 is involved in forward trafficking of
111 Ppk1 to dendrites, which indicates a role for endosome-mediated trafficking in both dendrite
112 growth and the delivery of a sensory ion channel. Together, our results suggest that Ppk
113 channel delivery is coordinated with sensory dendrite morphogenesis, thus revealing a
114 mechanism to establish proper ion channel levels and distribution throughout sensory dendrites.

Results

Ppk1 is enriched in dendrites and the dendritic membrane in developing sensory neurons

To visualize the localization of the Ppk ion channel in sensory neurons, we tagged endogenous Ppk1 with fluorescent proteins. To facilitate the manipulation of *ppk1*, we first replaced the ppk1 gene with an attP "docking site," which enables the reliable and rapid knock-in of new *ppk1* alleles (*Figure 1A*). We then used this strain to knock-in *ppk1* tagged with one copy of superfolder GFP (sfGFP) at either the N- or C-terminus (*Figure 1B and Figure 1—figure supplement 1*; since Ppk1 tagged with GFP at either terminus displayed similar localization, we used C-terminally tagged Ppk1 for most of our experiments). Excitingly, we observed fluorescent signal in neurons in live animals with just one copy of GFP attached to Ppk1 (*Figure 1B*). Consistent with previous reports, Ppk1::sfGFP was expressed in the class IV da neurons in the peripheral nervous system (Adams et al., 1998; Darboux et al., 1998; Grueber et al., 2002). In the dorsal class IV da neuron called ddaC, Ppk1::sfGFP localized to both dendrites and axons, but its distribution to and within these compartments differed. Ppk1::sfGFP was enriched in dendrites, where it appeared to localize predominantly to the dendritic membrane and was present throughout the dendritic arbor (*Figure 1B*). This distribution matches the previously reported distribution of Ppk1 based on antibody staining and fluorescently tagged Ppk1 transgenes (Ainsley et al., 2008; Gorczyca et al., 2014; Mauthner et al., 2014). In contrast to dendrites, the Ppk1::sfGFP signal was dimmer in axons and did not align with the axonal membrane (*Figure 1B*). In the ventral nerve cord, where the ddaC axons terminate, Ppk1::sfGFP was present in axon terminals (*Figure 1C*). Altogether, our data indicate that Ppk1::sfGFP localizes predominantly to dendrites, but that it is also present at low levels in axons and in axon terminals.

In addition to tagging Ppk1 with sfGFP, we also tagged Ppk1 with mCherry at the C-terminus. The distribution of Ppk1::mCherry was similar to Ppk1::sfGFP in dendrites and axons (*Figure 1D*). There was, however, a striking difference: unlike Ppk1::sfGFP, Ppk1::mCherry clustered in bright puncta that concentrated in the cell body, proximal dendrites, and axon (*Figure 1D, G*). These Ppk1::mCherry puncta were motile and moved at speeds consistent with microtubule-based transport (*Figure 1E*). This is in contrast with Ppk1::sfGFP, which was rarely visible in puncta (*Figure 1B*). Interestingly, the Ppk1 partner subunit Ppk26 tagged with the fluorescent

149 protein Dendra2 also displays a punctate distribution pattern similar to mCherry-tagged Ppk1,
150 whereas Ppk26 tagged with GFP resembles the more uniform distribution of GFP-tagged Ppk1
151 (Krämer et al., 2019; Mauthner et al., 2014). Unsure of whether the mCherry tag might direct
152 Ppk1 to a different compartment than sfGFP, we next generated Ppk1 tagged with both sfGFP
153 and mCherry (sfGFP::Ppk1::mCherry). The sfGFP and mCherry fluorescent signals of the dual-
154 tagged sfGFP::Ppk1::mCherry resembled those of the singly tagged Ppk1 proteins (*Figure 1F,*
155 *G*). This suggests that the punctate mCherry signal does not reflect a difference in the
156 localization of mCherry-tagged Ppk1. Rather, the mCherry tag may reveal the localization of
157 Ppk1 to a compartment(s) where sfGFP does not fluoresce. For example, among other
158 differences, sfGFP and mCherry have different maturation kinetics and are differentially
159 sensitive to pH (e.g., GFP fluorescence is quenched by low pH whereas mCherry is not)
160 (Chudakov et al., 2010). Our comparison of the fluorescent sfGFP and mCherry signals of the
161 dual-tagged Ppk1 indicates that the identity of the fluorescent protein tag can influence protein
162 visualization and that using different fluorescent tags may be necessary to visualize the full
163 potential range of a protein's localization in cells.
164
165 The localization of fluorescently tagged Ppk1 to both axons and dendrites raises the question of
166 where Ppk1 is inserted into the membrane. To monitor the membrane localization of Ppk1, we
167 initially tagged Ppk1 with superecliptic pHluorin. Superecliptic pHluorin is a pH-sensitive GFP
168 variant that is often used to monitor the insertion of transmembrane proteins because it
169 fluoresces in neutral pH environments, such as extracellular space, but has minimal
170 fluorescence in low pH environments, such as the lumen of a transport vesicle (Miesenböck et
171 al., 1998). To determine an optimal position at which to add a fluorescent tag such as pHluorin,
172 we first tagged an extracellular loop of endogenous Ppk1 with sfGFP and compared its
173 fluorescence to Ppk1 tagged with sfGFP at the N- or C-terminus. We tested two positions in an
174 extracellular (EC) loop: Site 1 was selected based on the structure of chicken ASIC1, and Site 2
175 is a position that was previously used to monitor rat ASIC1a membrane insertion via a
176 haemagglutinin epitope tag (Chen and Gründer, 2007) (*Figure 2—figure supplement 1*). We
177 found that insertion of sfGFP at Site 1 resulted in fluorescence similar to Ppk1::sfGFP, whereas
178 the insertion of sfGFP at Site 2 led to relatively weak fluorescence (*Figure 2—figure supplement*
179 *1*). We then tagged Ppk1 with pHluorin at Site 1 and found that Ppk1::pHluorin^{EC} produced
180 relatively weak fluorescence (*Figure 2—figure supplement 2A*). We next tested the effects of
181 eliminating Ppk26 on Ppk1::pHluorin^{EC} fluorescence and distribution, as the loss of Ppk26
182 should interfere with the membrane localization of Ppk1. In *ppk26* mutant neurons,

183 Ppk1::pHluorin^{EC} fluorescence noticeably increased in the cell body and decreased in dendrites,
184 but fluorescence was still clearly visible in patches in dendrites, particularly at dendrite branch
185 points (*Figure 2—figure supplement 2B*). Given that the membrane localization of Ppk1
186 depends on Ppk26, the fluorescence pattern of Ppk1::pHluorin^{EC} in the *Ppk26* mutant neurons
187 suggested that Ppk1::pHluorin^{EC} might fluoresce in the neutral environment of the endoplasmic
188 reticulum (ER) as well as in the cell membrane. The potential for Ppk1::pHluorin^{EC} to fluoresce
189 in both the ER and cell membrane limits its use as a tool to monitor the insertion of Ppk1 into
190 the neuronal membrane.
191
192 The weak fluorescent signal of Ppk1::pHluorin^{EC}, and its ability to fluoresce in the ER, led us to
193 develop a new split-GFP approach to monitor the membrane insertion of endogenous Ppk1
194 (*Figure 2A*). This approach is analogous to other recently reported split-GFP techniques to
195 monitor the localization of transmembrane proteins (Ji et al., 2022; Kamiyama et al., 2021). We
196 tagged endogenous Ppk1 at Site 1 in the extracellular loop with three copies of the split-GFP
197 peptide GFP(11). In addition to the extracellular GFP(11) tag, we also tagged the Ppk1 C-
198 terminus with mCherry, which enabled us to follow Ppk1 localization throughout the neuron
199 (Ppk1::GFP(11x3)^{EC}::mCherry$^{C\text{-}term}$). We then expressed a secreted version of GFP(1-10)
200 (secGFP(1-10)) in fat cells, which released secGFP(1-10) into the hemolymph of the larval open
201 circulatory system. Thus, Ppk1 tagged with GFP(11) in an extracellular loop will only fluoresce
202 when Ppk1 is inserted into the cell membrane and encounters secGFP(1-10) (*Figure 2—figure*
203 *supplement 3*). As a control, we used a construct in which the extracellular N-terminus of the
204 single-pass transmembrane protein CD4 is tagged with GFP(11) and the C-terminus is tagged
205 with tdTomato (GFP(11)^{EC}::CD4::tdTomato) (*Figure 2—figure supplement 4*) (Han et al., 2012).
206
207 Using this split-GFP approach, we monitored GFP fluorescence from Ppk1 and CD4 tagged
208 with GFP(11). Both Ppk1::GFP(11x3)^{EC}::mCherry$^{C\text{-}term}$ and GFP(11)^{EC}::CD4::tdTomato exhibited
209 GFP fluorescence in dendrites and cell bodies (*Figure 2B-D, Figure 2—figure supplement 4*). As
210 described above, the membrane localization of Ppk1 depends on Ppk26 (Gorczyca et al., 2014;
211 Guo et al., 2014; Mauthner et al., 2014). In neurons lacking Ppk26, there was no GFP
212 fluorescent signal from Ppk1::GFP(11x3)^{EC}::mCherry$^{C\text{-}term}$, albeit the mCherry signal was still
213 visible, indicating that Ppk1 was still produced in the absence of Ppk26 (*Figure 2B*). These
214 results support the idea that GFP fluorescence results from Ppk1 insertion into the dendritic
215 membrane.
216

217 Next, we examined axons and axon terminals. Strikingly, in neurons expressing Ppk1 tagged
218 with GFP(11), we observed a distinct boundary of GFP fluorescence between the cell body and
219 proximal axon, the latter of which was devoid of fluorescent signal (*Figure 2D*). While the
220 proximal axon and axon shaft lacked GFP fluorescence, we observed GFP fluorescence in the
221 axon terminals of neurons expressing Ppk1::GFP(11x3)^{EC}::mCherry$^{C\text{-}term}$ (*Figure 2E*). The
222 peripheral axons and ventral nerve cord are wrapped by glia, which form a barrier that is
223 unlikely to be penetrated by secGFP(1-10) (Banerjee, 2006; Freeman, 2015; Stork et al., 2008).
224 Thus, the GFP fluorescence from Ppk1 tagged with GFP(11) potentially reflects the trans-
225 endocytosis of Ppk1 from the somatodendritic compartment to the axon terminals.
226
227 In contrast to Ppk1 tagged with GFP(11), CD4 tagged with GFP(11) displayed GFP
228 fluorescence throughout the proximal axon and axon shaft (*Figure 2D*). This indicates a
229 difference in the membrane localization of endogenous Ppk1 and CD4. In summary, we have
230 developed a new assay to monitor the neuronal membrane localization of Ppk1, which we have
231 used to reveal that Ppk1 is inserted into the somatodendritic membrane and the axon terminal
232 membrane but not the membrane in the proximal axon or axon shaft.
233
234
235 **Ppk1 is present in dendritic branches as they form and extend**
236
237 The localization of Ppk1 and Ppk channels throughout the dendritic arbor raises the question of
238 how Ppk1 becomes so broadly localized. One possibility is that Ppk1 is delivered to dendrites at
239 the same time that the arbor is established, and thus Ppk1 distribution may be coordinated with
240 dendrite growth. To determine the localization of Ppk1 relative to when they develop, we
241 examined the early expression of Ppk1. *ppk1* expression is reported to initiate during embryonic
242 stages, slightly before dendrites emerge (~embryonic stage 16) (Adams et al., 1998; Darboux et
243 al., 1998; Gorczyca et al., 2014; Jaszczak et al., 2022; Zelle et al., 2013). Indeed, we first
244 observed Ppk1::sfGFP in cell bodies and proximal axons just prior to dendrite extension, and we
245 even observe Ppk1::sfGFP in newly emerging dendrites (*Figure 3A*). These data indicate that
246 Ppk1 is expressed from the very beginning of dendritogenesis.
247
248 Next, we asked whether Ppk1 is present in growing dendrites. Since imaging Ppk1::sfGFP
249 during embryonic stages was technically challenging, we followed the real-time localization of
250 Ppk1::sfGFP in both newly formed and extending dendrite branches in larvae. Strikingly,

251 Ppk1::sfGFP was present throughout growing dendrite branches, in both branches that formed
252 *de novo* and branches that extended (*Figure 3B*). We imaged Ppk1::sfGFP both continuously
253 and over a period of several minutes, and at both time scales we consistently observed
254 Ppk1::sfGFP throughout dendrite branches as they grew and, in some instances, retracted. We
255 also imaged Ppk1 tagged with GFP(11) and observed GFP fluorescence in growing dendrite
256 branches, which indicates that Ppk1 is integral to the membrane of growing dendrite tips (*Figure*
257 *3C*). Altogether, these data indicate that Ppk1 is present in growing dendrites.
258
259 We next asked whether the broad distribution of Ppk1 throughout the dendritic arbor and in
260 growing dendrites might reflect its ability to readily diffuse in the dendritic membrane. To test
261 this we carried out fluorescence recovery after photobleaching (FRAP) with GFP(11)-tagged
262 Ppk1 and CD4 (Ppk1::GFP(11x3)^{EC}::mCherry$^{C\text{-term}}$ and GFP(11)^{EC}::CD4::tdTomato,
263 respectively). After photobleaching, GFP fluorescence from Ppk1::GFP(11x3)^{EC}::mCherry$^{C\text{-term}}$
264 recovered gradually over tens of minutes, significantly slower than GFP(11)^{EC}::CD4::tdTomato
265 (*Figure 3D*). These FRAP results indicate that rapid diffusion of Ppk1 is unlikely to explain its
266 broad distribution and presence in growing dendrites.
267
268 Our findings that Ppk1 is present in growing dendrites raises the question of whether Ppk1, and
269 its partner subunit Ppk26, are necessary for dendrite growth and whether any change in Ppk
270 channel activity might perturb dendrite morphogenesis. In neurons lacking both Ppk1 and
271 Ppk26, dendrite growth was normal (*Figure 3E*). Although the Ppk channel is not essential for
272 dendrite growth, we found, consistent with previous reports, that dendrite arborization is
273 reduced when Ppk channel activity is altered by a degenerin mutation in Ppk26, which keeps
274 the channel in an aberrant open state (*Figure 3—figure supplement 1A*) (Bianchi, 2022; Bianchi
275 et al., 2004; Brown et al., 2007; Gorczyca et al., 2014). Surprisingly, the loss of Ppk1 enhanced,
276 rather than suppressed, the reduction in dendrite arborization associated with the mutant Ppk26
277 (*Figure 3—figure supplement 1B*). This suggests that the Ppk26 degenerin mutant does not
278 depend on Ppk1 to form a functional channel and that Ppk1 may restrain the activity of the
279 mutant Ppk26. Our data also suggest that either the mutant Ppk26 may be able to reach the
280 dendritic membrane independently of Ppk1 or that the dendrite growth defect caused by the
281 Ppk26 degenerin mutant is due to the aberrant activity of Ppk26 in an internal organelle.
282 Combined, our results indicate that while Ppk1 and Ppk26 are dispensable for normal dendrite
283 growth, Ppk channel activity must be tightly regulated to achieve proper dendrite arborization.
284

285

286 **Ppk1 levels are not affected by decreasing dendrite arbor size but are reduced when**
287 **dendrite length significantly increases**

288

289 Our data reveal that Ppk1 is present in the membrane of extending dendrite branches. One
290 potential model based on these data is that Ppk1 is transported to dendrites via the membrane
291 that grows the dendritic arbor. Since we were not able to visualize the transport of fluorescently
292 tagged Ppk1 in growing dendrites, we instead considered the predictions of this model. One
293 prediction of the model that Ppk1 is transported to dendrites with the membrane that grows the
294 arbor is that the dendritic levels of Ppk1 should be proportional to the amount of dendritic
295 membrane or, in other words, dendrite size. We tested this by assessing Ppk1 levels when
296 dendrite arbor size was altered. We took advantage of different conditions that are known to
297 reduce or increase dendrite growth, acknowledging that these experiments could only serve as
298 a general test of whether Ppk1 levels are proportional to dendrite arbor size. First, we tested two
299 different conditions that reduce dendrite growth: knock-down of the ribosomal protein Rpl22 and
300 overexpression of the ecdysone receptor (EcR) (Lin et al., 2015; Ou et al., 2008). Under both
301 conditions, Ppk1::sfGFP density in dendrites was similar to controls, supporting the idea that
302 Ppk1 levels were proportional to arbor size when dendrite growth was reduced by these two
303 manipulations (*Figure 4A, B*). We then determined whether Ppk1 levels would change when
304 dendrite growth increased using the overexpression of the actin regulator Rac1 (Emoto et al.,
305 2004) and the overexpression of phosphoinositide 3-kinase (PI3K), which regulates cell growth
306 through the mTOR (mechanistic target of rapamycin) pathway (Parrish et al., 2009). As
307 previously reported, Rac1 overexpression increased dendrite branch number without affecting
308 dendrite length, and we found that Ppk1::sfGFP levels were not affected (*Figure 4C*).
309 Overexpression of PI3K increased both dendrite branch number and dendrite length by
310 approximately a third, and, in contrast to the other growth-perturbing conditions, Ppk1::sfGFP
311 levels were reduced by nearly a third (*Figure 4D*). In this overgrowth condition it is possible that
312 the production of Ppk1::sfGFP is outpaced by dendrite growth. Although this is only a small
313 sampling of the many conditions that affect dendrite growth, our results suggest that the
314 dendritic levels of Ppk1 are not generally altered by perturbing dendrite growth.

315

316

317 **Ppk1 persists in dendrites when dynein-mediated transport is perturbed**

318

319 We further tested the model that Ppk1 is transported to dendrites via the membrane that grows
320 the dendritic arbor by disrupting transport to dendrites. We reasoned that if Ppk1 is trafficked via
321 the membrane that fuels dendrite growth, then perturbing transport to dendrites should
322 decrease growth and have a proportional effect on the dendritic levels of Ppk1 (e.g., the density
323 of Ppk1 should not be affected).
324
325 We took several complementary approaches to determine the effects of disrupting dendritic
326 transport on Ppk1. Most transport to and within dendrites occurs along microtubules. In da
327 neuron dendrites, nearly all microtubules are oriented with their minus-ends positioned away
328 from the cell body (Rolls, 2011). Thus, the microtubule minus-end-directed motor dynein is
329 thought to mediate the majority of transport to dendrites. We perturbed dynein function in
330 several ways. First, we reduced the levels of the essential dynein subunit dynein light
331 intermediate chain (Dlic) via RNAi. In *Dlic-RNAi*-expressing neurons, we observed a reduction in
332 dendrite growth as previously reported (Satoh et al., 2008; Zheng et al., 2008), but dendritic
333 Ppk1::sfGFP levels were similar to controls (*Figure 5A*). Consistent with these results, we found
334 that loss of the dynein co-factor nudE, which also disrupts dendrite morphogenesis (Arthur et
335 al., 2015), did not affect the dendritic levels of Ppk1::sfGFP (control: 112.77 ± 21.05 arbitrary
336 units [AU]; *nudE*^{39A}/*Df(3L)BSC673*: 110.52 ± 42.55 AU, mean ± standard deviation; Student's
337 unpaired t-test: p=0.8382; not significant). Thus, decreasing dynein activity reduced dendrite
338 growth, likely reflecting its role in dendritic transport, but Ppk1 levels in dendrites were
339 unchanged. These results indicate that Ppk1 levels remain proportional to dendrite arbor size in
340 dynein loss-of-function neurons.
341
342 We also disrupted dynein activity by overexpressing dynamitin (dmn), a dynein co-factor and
343 dynactin complex member. Elevating dmn levels disrupts dynein activity, likely by perturbing
344 dynein-dynactin interactions (Echeverri et al., 1996; Schroer, 2004). Unlike *Dlic-RNAi* and *nudE*
345 loss-of-function, the overexpression of *dmn* reduced dendritic levels of Ppk1::sfGFP by
346 approximately a quarter (*Figure 5B*). Since overexpressed dmn acts as a dominant-negative, it
347 may exert a stronger, cumulative effect on dynein-mediated transport than *Dlic-RNAi* and the
348 *nudE* loss-of-function mutant. Indeed, when we examined younger larvae, neurons
349 overexpressing *dmn* had normal levels of Ppk1::sfGFP (*Figure 5B*). Such a dose-dependent
350 effect may also explain why we previously observed reduced dendritic Ppk1 levels in clones of
351 *dlic* mutant neurons, which completely lack *dlic* (Zheng et al., 2008). Our results indicate that the
352 overexpression of *dmn* initially had no effect on Ppk1::sfGFP levels in dendrites but that the

353 persistent overexpression of *dmn* resulted in the decrease of Ppk1::sfGFP dendritic levels over
354 time.
355
356 Our findings that the dendritic levels of Ppk1 are not affected by either *Dlic-RNAi* or *nudE* loss-
357 of-function could be interpreted to suggest that Ppk1 is not transported by dynein. To determine
358 whether dynein plays a role in transporting Ppk1 to dendrites, we took a closer look at neurons
359 expressing *Dlic-RNAi*. Most ion channels traffic through the Golgi apparatus, which, in the da
360 neurons, includes both the somatic Golgi and dendritic Golgi "outposts," which are Golgi mini-
361 stacks found predominantly in the proximal dendritic arbor (Gardiol et al., 1999; Horton and
362 Ehlers, 2003; Yang and Wildonger, 2020; Ye et al., 2007; Zhou et al., 2014). In control neurons,
363 we found that Ppk1::sfGFP co-localized with somatic Golgi, although we did not detect any
364 Ppk1::sfGFP at dendritic Golgi outposts (*Figure 5C*). In neurons expressing *Dlic-RNAi*,
365 Ppk1::sfGFP accumulated at somatic Golgi and could also be observed at dendritic Golgi
366 outposts. These results suggest that Ppk1 traffics through both somatic Golgi and Golgi
367 outposts and that Ppk1 is transported away from Golgi by dynein.
368
369 In addition to dendritic defects, neurons with altered dynein activity had increased levels of
370 Ppk1::sfGFP in axons (*Figure 5A, B*). Previous work by our group and others has shown that
371 Golgi and Golgi outposts mis-localize to axons when dynein activity is altered (Arthur et al.,
372 2015; Zheng et al., 2008). Given our findings that Ppk1::sfGFP accumulates at Golgi in dynein
373 loss-of-function neurons, one possibility is that Ppk1::sfGFP "hitchhikes" on Golgi that are
374 ectopically localized to axons. However, in the axons of *Dlic-RNAi*-expressing neurons,
375 Ppk1::sfGFP was often adjacent to, but did not overlap with, the trans-Golgi marker
376 GALNT2::TagRFP (*Figure 5D*). Although Ppk1 was not hitchhiking on Golgi, it was still possible
377 that the mis-localization of Golgi was responsible for the increase in axonal Ppk1 levels. To test
378 this, we perturbed the localization of Golgi by disrupting the golgin lava lamp (lva), which links
379 Golgi to dynein but otherwise does not contribute to dynein activity (Papoulas et al., 2004;
380 Sisson et al., 2000). Consistent with previous reports, we found that the overexpression of
381 dominant-negative lva resulted in the ectopic axonal localization of Golgi (Ye et al., 2007). Lva
382 dominant-negative also resulted in an increase in Ppk1::sfGFP levels in axons and the cell body
383 (*Figure 5E*). Combined, our results suggest that the mis-localization of Golgi in dynein loss-of-
384 function neurons is sufficient to result in the accumulation of Ppk1 in axons.
385
386

387 **Disrupting secretory pathway function impedes the delivery of Ppk1 to the dendritic**
388 **membrane**
389
390 Our finding that Ppk1 accumulates at Golgi when dynein function is perturbed indicates that
391 Ppk1 traffics through the Golgi, likely through both the somatic Golgi and Golgi outposts, before
392 being added to the growing dendritic membrane. Based on these data, we hypothesized that
393 interfering with the function of the secretory pathway, which is the predominant source of
394 membrane for dendrite arbor growth and through which membrane proteins traffic, might reduce
395 the dendritic levels of Ppk1. We disrupted secretory pathway function by impeding the budding
396 of cargo-containing vesicles from the ER. We used a transgenic guide RNA (gRNA) that targets
397 *Sec23*, which encodes an essential component of the COPII vesicular coat, in combination with
398 a transgene that expresses Cas9 specifically in the class IV da neurons (Poe et al., 2018). The
399 *Sec23* gRNA targets the first coding exon of *Sec23* and, in combination with Cas9, is predicted
400 to generate a loss-of-function allele by introducing a premature stop in Sec23. Indeed, neurons
401 expressing *Sec23* gRNA and Cas9 had shorter dendrites and fewer branches, consistent with
402 previously published work that *Sec23* loss-of-function reduces dendrite morphogenesis (*Figure*
403 *6A*) (Ye et al., 2007).
404
405 Next, we examined the effects of *Sec23* loss-of-function on Ppk1. *Sec23* loss-of-function
406 neurons had significantly less membrane-associated Ppk1 as revealed by a reduction in GFP
407 fluorescence from the dual-tagged Ppk1::GFP(11x3)^{EC}::mCherry$^{C\text{-}term}$ (*Figure 6B*). The mCherry
408 fluorescence of Ppk1::GFP(11x3)^{EC}::mCherry$^{C\text{-}term}$ was also reduced, but to a lesser extent than
409 the GFP fluorescence. This suggests that disrupting *Sec23* has only a modest effect on Ppk1
410 levels but has a severe effect on the trafficking of Ppk1 to the neuronal membrane. Consistent
411 with this idea, the dendritic levels of Ppk1::sfGFP were not affected in *Sec23* loss-of-function
412 neurons, although the pattern of Ppk1::sfGFP appeared patchy compared to its typical uniform
413 distribution in control neurons (*Figure 6C*). Notably, both the mCherry fluorescence of
414 Ppk1::GFP(11x3)^{EC}::mCherry$^{C\text{-}term}$ and the Ppk1::sfGFP fluorescence appeared greatly
415 increased in the cell bodies (*Figure 6B, C*). Combined, these results suggest that perturbing
416 *Sec23* results in dramatically less membrane-associated Ppk1 and likely causes an
417 accumulation of Ppk1 at an early point during the secretory pathway, likely the ER.
418
419
420 **Dendritic levels of Ppk1 are reduced by disrupting Rab11**

421
422 We next asked what transport carriers might take Ppk1 from Golgi to growing dendrites and play
423 a role in coordinating ion channel delivery with dendrite growth. We considered Rab11-positive
424 endosomes for several reasons. First, Rab11 has been implicated in the anterograde trafficking
425 of ion channels to the dendritic membrane in mammalian neurons (Bowen et al., 2017), and
426 recent work suggests that Rab11 may affect the trafficking of the Ppk1 partner subunit Ppk26 in
427 fly da neurons (Krämer et al., 2019). Additionally, Rab11 plays a role in the membrane
428 localization of ENaC family members in the epithelial cells of mammalian kidneys (Butterworth
429 et al., 2012; Karpushev et al., 2008; Ware et al., 2020). Rab11 mutants also reduce dendrite
430 arborization, indicating that it has a role in dendrite growth (*Figure 7—figure supplement 1*)
431 (Krämer et al., 2019; Lin et al., 2020). These data suggest that Rab11 may play a role in both
432 the dendritic localization of Ppk1 and dendrite arbor development.
433
434 To test whether Rab11 indeed participates in trafficking Ppk1 to dendrites, we perturbed Rab11
435 function using both *Rab11-RNAi* and a dominant-negative Rab11 construct, Rab11-DN (Rab11-
436 DN carries an S25N mutation that disrupts GTPase activity). Knocking-down Rab11 with RNAi
437 decreased dendritic Ppk1 as determined by measuring Ppk1 membrane levels via
438 immunohistochemistry, Ppk1::sfGFP, and Ppk1::mCherry (Ppk1 membrane expression was
439 assayed with antibodies rather than GFP(11)-tagged Ppk1 for technical reasons; *Figure 7A-C*).
440 In neurons expressing *Rab11-RNAi*, the decrease in Ppk1 in dendrites was accompanied by an
441 accumulation of Ppk1::sfGFP and Ppk1::mCherry in cell bodies (*Figure 7B, C*). Similar to
442 *Rab11-RNAi*, the overexpression of Rab11-DN also reduced Ppk1 levels in dendrites as
443 revealed by quantifying Ppk1 membrane expression via immunohistochemistry and
444 Ppk1::mCherry (Rab11-DN is tagged with GFP, and thus we were not able to quantify
445 Ppk1::GFP; *Figure 7D, E*). Like in neurons expressing *Rab11-RNAi*, Ppk1::mCherry
446 accumulated in the cell body in *Rab11-DN*-expressing neurons (*Figure 7E*). Together, these
447 results indicate that the disruption of Rab11 leads to a decrease in Ppk1 levels in dendrites and
448 an accumulation of Ppk1 in the cell body.
449
450 Our findings are consistent with the idea that Rab11 participates in transporting Ppk1 from Golgi
451 to dendrites, but Rab11 also plays a role in the local recycling of ion channels in dendrites
452 (Hausser and Schlett, 2017). We next asked whether dendritic Ppk1 levels might be regulated
453 via local recycling. In addition to Rab11, which functions in late recycling endosomes, local
454 recycling of ion channels depends on the early endosome GTPase Rab5 (Hausser and Schlett,

455 2017). We found that dendritic Ppk1::mCherry puncta colocalized with Rab5-positive early
456 endosomes, as did some Ppk1::mCherry puncta in the cell body, which suggests that Rab5 may
457 play a role in trafficking Ppk1 (*Figure 8A*).
458
459 We next analyzed the effects of perturbing Rab5 function on dendritic levels of Ppk1 using a
460 dominant-negative Rab5 construct, Rab5-DN (Rab5-DN carries a S43N mutation that disrupts
461 GTPase activity). The overexpression of Rab5-DN did not disrupt dendritic levels of Ppk1 as
462 measured by quantifying Ppk1 dendritic membrane levels via immunohistochemistry and
463 Ppk1::mCherry (because Rab5-DN is tagged with YFP, we did not quantify GFP-tagged Ppk1)
464 (*Figure 8B, C*). Thus, although Rab5-DN reduces dendrite growth similar to Rab11-DN and
465 *Rab11-RNAi* (*Figure 7—figure supplement 1, Figure 8—figure supplement 1A*), Rab5-DN has
466 no effect on dendritic Ppk1 levels. Strikingly, although the dendritic levels of Ppk1::mCherry
467 were not affected by Rab5-DN, the number of Ppk1::mCherry puncta in the proximal dendrites
468 and cell body were significantly reduced, and, in many neurons, virtually eliminated (*Figure 8C*).
469 This suggests that Ppk1::mCherry puncta likely represent Ppk1 in endosomes, specifically early
470 endosomes whose formation depends on Rab5 function. Indeed, consistent with previous
471 reports, we observed that fluorescently tagged Rab5-DN appeared diffuse, which differed from
472 the punctate distribution pattern of fluorescently tagged wild-type Rab5 (*Figure 8—figure*
473 *supplement 1B*) (Zhang et al., 2007). While this change in Rab5-DN distribution could reflect its
474 dissociation from early endosomes, it might also indicate that early endosome formation is
475 impaired in Rab5-DN-expressing neurons. Overall, our results suggest that Ppk1 traffics through
476 Rab5-positive endosomes but that this trafficking does not have a significant effect on dendritic
477 levels of Ppk1. Combined, our results suggest that Rab11 participates in the forward trafficking
478 of Ppk1 to dendrites at the same time that it promotes dendrite growth.

Discussion

The perception of stimuli by sensory neurons depends on the morphogenesis of a dendritic arbor equipped with ion channels and receptors that will detect sensory inputs. Central outstanding questions have been: How are ion channels and receptors localized to sensory neuron dendrites during development, and how does a sensory neuron properly match ion channel and receptor levels with dendrite arbor size? Sensory dendrites lack synaptic input, which has made it unclear whether known mechanisms of ion channel and receptor trafficking to dendrites with synapses would also regulate the delivery of ion channels and receptors to the asynaptic dendrites of sensory neurons. Our studies of the localization of Ppk1 suggest a model in which sensory neurons likely package ion channels into the membrane that grows the dendritic arbor, thus coordinating the delivery of ion channels with arbor expansion.

Our data reveal that Ppk1 is present throughout the membrane of dendrites as they grow, indicating that Ppk channels are an integral component of both newly formed and extending dendrites. While the localization and function of ion channels in growing axons is well established (Ehlers et al., 1998; Gill et al., 2014; Herkert et al., 1998; Kerstein et al., 2015; Liu et al., 2020; Schenk et al., 2003; Wang et al., 2011), little is still known about the localization and function of ion channels in developing dendrites. The timing and breadth of Ppk1 distribution indicates that the class IV da sensory dendrites are likely equipped with the capacity to detect stimuli as soon as dendrites emerge. Indeed, recent work has implicated members of the *C. elegans* DEG/ENaC family in sensing mechanical forces to promote terminal branch growth during arbor formation in PVD neurons (Tao et al., 2022). Although we found that dendrite development occurred normally without Ppk1 and its partner subunit Ppk26, it is nonetheless possible that Ppk channels participate in dendrite growth, possibly in collaboration with another (mechanosensory) ion channel. Class IV da neurons express at least one additional mechanosensory channel, Piezo, whose worm ortholog is only weakly expressed in PVD neurons. In vertebrate neurons, the distribution of ion channels in young dendrites has been reported but is not well characterized, although a rich body of work supports the role of activity in regulating dendrite growth (Craig et al., 1993; Rao et al., 1998; Wong and Ghosh, 2002). Our visualization of fluorescently tagged endogenous Ppk1 provides evidence that ion channels are indeed part of the growing dendritic membrane, similar to the localization of ion channels in axons, and that sensory dendrites thus have a "built in" capacity to detect stimuli.

513 The presence of Ppk1 in growing dendrites raises the possibility that Ppk channels are
514 transported to dendrites as part of the membrane that fuels arbor growth. In one test of this
515 model, we disrupted transport to dendrites by interfering with dynein. Dynein is the predominant
516 motor for dendritic transport in da neurons, and perturbing dynein function significantly reduces
517 arbor size (Satoh et al., 2008; Zheng et al., 2008). We found that the dendritic levels of
518 Ppk1::sfGFP remained normally proportional to arbor size in neurons with reduced dynein
519 activity. This suggests that in dynein loss-of-function neurons, the membrane that does make it
520 to dendrites has normal levels of Ppk1. The finding that Ppk1::sfGFP accumulates at Golgi in
521 dynein loss-of-function neurons indicates that dynein normally transports Ppk1 (and Ppk
522 channels) from Golgi to dendrites. Our results, combined with previous studies (Satoh et al.,
523 2008), suggest that interfering with dynein function reduces the amount of membrane that is
524 added to the arbor over time but does not affect the amount of Ppk1 that is packaged into the
525 membrane destined for dendrites. Thus, interfering with dynein activity perturbs dendrite
526 arborization but does not affect Ppk1 density. Strikingly, even interfering with translation via the
527 knockdown of the ribosomal protein RpL22, which decreases dendrite growth, does not affect
528 dendritic levels of Ppk1. This result is also consistent with the idea that Ppk1 and Ppk channels
529 are packaged into transport packets at a consistent density even if their subsequent transport
530 out of the Golgi is disrupted. Moreover, our analysis of Ppk1::sfGFP levels in dendrite growth
531 mutants, coupled with published reports of Ppk1 or Ppk26 in mutants that affect arbor size, also
532 indicate that Ppk levels typically remain constant or are only minimally affected despite dramatic
533 changes in dendrite arbor size (Hu et al., 2020; Rui et al., 2020; Ziegler et al., 2017). The idea
534 that Ppk1 and Ppk channels are transported to dendrites via the membrane that grows
535 dendrites suggests a mechanism for the coordination of ion channel levels and dendrite arbor
536 size.
537
538 Once Ppk1 reaches the dendrites, our FRAP analysis of membrane-localized Ppk1
539 (Ppk1::GFP(11)^{EC}) suggests that Ppk channels remain stably inserted into the dendritic
540 membrane with little baseline turnover. This idea is also supported by our finding that Ppk1
541 levels are not significantly affected when local protein recycling is disrupted via the expression
542 of Rab5-DN. Moreover, our FRAP analysis of Ppk1::GFP(11)^{EC} did not uncover any hot spots of
543 fluorescent signal recovery that might indicate areas of ion channel addition, although it is
544 possible that such sites of insertion are below our level of detection. Recent qRT-PCR analysis
545 has revealed that Ppk1 mRNA levels drastically decrease after the 2nd instar developmental
546 stage (Jaszczak et al., 2022), which corresponds to when dendrite growth slows significantly

547 (Parrish et al. 2009). These data, combined with our FRAP results, suggest that Ppk1 is stably
548 integrated into the dendritic membrane as dendrites grow expansively, and, once dendrite
549 growth plateaus, there is little replenishment with newly expressed Ppk1.
550
551 To monitor the membrane localization of Ppk1, we used a novel split-GFP approach. These
552 experiments revealed that Ppk1 is present throughout the somatodendritic membrane but not
553 the membrane of the proximal axon or axon shaft. The clear demarcation of Ppk1::GFP(11)^{EC}
554 fluorescent signal between the somatodendritic and axonal compartments is consistent with the
555 presence of a diffusion barrier between these two compartments in the proximal axon of fly
556 neurons, as was previously supported by studies of the fly ankyrin Ank2 (Jegla et al., 2016;
557 Leterrier, 2018; Winckler et al., 1999). Although there is a barrier to the diffusion of Ppk1 from
558 the somatodendritic membrane to the axonal membrane, Ppk1 is not prevented from being
559 trafficked into the axon to the axon terminal. Given that ensheathing glia likely exclude
560 secGFP(1-10) (Banerjee, 2006; Freeman, 2015; Stork et al., 2008), the Ppk1::GFP(11)^{EC}
561 fluorescent signal at axon terminals may reflect the trans-endocytosis of Ppk1 from dendrites to
562 axons. It is not clear what role Ppk1 may play in the axon terminals of class IV da neurons,
563 although other studies, including in flies, support presynaptic roles for Ppk channels and their
564 orthologs (Bianchi, 2022; Kellenberger and Schild, 2002; Younger et al., 2013). Additional
565 studies will be needed to determine whether Ppk1 is preferentially trafficked to one
566 compartment or the other and whether Ppk1 may be stably inserted into the dendritic, but not
567 axonal, membrane. Ppk1::GFP(11)^{EC} provides a tool to investigate the spatially restricted
568 membrane expression of Ppk1 and the diffusion barrier between the somatodendritic and
569 axonal membranes.
570
571 Our data indicate that Rab11 plays a role in the transport of Ppk1 to dendrites. Rab11 is an
572 integral component of recycling endosomes but has also been implicated in the anterograde
573 trafficking of receptors and ion channels, including ENaCs, in neuronal and non-neuronal cells
574 (Ang et al., 2004; Bowen et al., 2017; Cresawn et al., 2007; Lock and Stow, 2005; Ware et al.,
575 2020). Our results implicate Rab11 in the forward transport of Ppk1 in fly da neurons, which
576 points to the potential conservation of DEG/ENaC/ASIC trafficking pathways across organisms
577 and cell types. Our results indicate that disrupting Rab11 reduces Ppk1 in dendrites but that
578 disrupting the function of Rab5, which acts in early endosomes, does not. This suggests that the
579 effects of perturbing Rab11 on Ppk1 is not due to an effect on Rab11-mediated recycling but is
580 likely due to a disruption of Rab11-mediated forward trafficking of Ppk1 to dendrites. Consistent

581 with this model, Ppk1 levels increase in the cell body when Rab11 levels or function are
582 perturbed. Recently, another group has also found that Ppk26 levels also increase in the cell
583 bodies of neurons with altered Rab11 (Krämer et al., 2019). It is notable that disrupting Rab11
584 does not lead to a total loss of Ppk1 from dendrites. This may be due to incomplete perturbation
585 of Rab11 or Rab11-positive endosomes, or it could indicate a complementary pathway for the
586 transport of Ppk1 and Ppk channels to dendrites. The pathways that supply membrane and
587 membrane proteins to dendrites, particularly growing dendrites, are still poorly understood. Our
588 data suggest that Rab11 and Rab11-positive endosomes may participate in a pathway that
589 coordinates Ppk ion channel delivery and dendrite arbor expansion.

590 **Materials and Methods**

591

592 Fly husbandry and stocks

593 Fruit flies were maintained at 25˚C on cornmeal-molasses-yeast medium. The generation of
594 new *ppk1* alleles and the *UAS-secGFP(1-10)* flies are described below. *ppk26* strains including
595 *ppk26*$^{\Delta 11}$, *UAS-ppk26::mCherry*, and *UAS-ppk26-DEG(A547V)::mCherry* were gifts of Dr. Yuh
596 Nung Jan (UCSF) (Gorczyca et al., 2014). The following alleles and transgenic fly strains from
597 the Bloomington Drosophila Stock Center (BDSC), Vienna Drosophila Resource Center
598 (VDRC), and individual laboratories were used: *ppk-Cas9* (Poe et al., 2018), *Df(3L)BSC673*
599 (BDSC 26525), *ppk-CD4::tdTomato* (BDSC 35845), *ppk-GFP(11)*^{EC}*::CD4::tdTomato* (Han et al.,
600 2012), *hsp70-Cre* (BDSC 1092), *DcG-Gal4* (Suh et al., 2006), *UAS-Dcr-2* (BDSC 24650), *UAS-*
601 *Dlic-RNAi* (VDRC 41686), *UAS-dynamitin* (BDSC 8784), *UAS-EcR-DN* (BDSC 9449), *UAS-*
602 *GALNT2::TagRFP* (BDSC 65253), *UAS-sfGFP(1-10)* (Bo Huang, UCSF), *UAS-Lva-DN* (BDSC
603 55055), *nudE*^{39A} (Wainman et al., 2009), *Ppk-Gal4* (BDSC 32078, BDSC 32079), *UASp-Rab5-*
604 *WT::YFP* (BDSC 24616), *UASp-Rab5-DN[S43N]::YFP* (BDSC 9772), *UAS-GFP::Rab5* (BDSC
605 43336), *UAS-PI3K* (BDSC 8294), *UAS-Rab11-RNAi* (VDRC 108382), *UAS-Rab11-DN(3-*
606 *4)::GFP* (Hsiu-Hsiang Lee, National Taiwan University College of Medicine), *UAS-Rac1* (BDSC
607 6293), *UAS-RpL22 RNAi* (BDSC 34828), *U6-Sec23-gRNA* (BDSC 79400), *w*^{1118}.

608

609

610 Generation of *ppk1* alleles

611 The endogenous *ppk1* gene (~3.7 kb encompassing the entire *ppk1* transcript) was knocked-out
612 and replaced with an attP site to facilitate the reliable integration of new *ppk1* alleles. The
613 *ppk1*$^{attP\text{-}KO}$ strain was generated using CRISPR-Cas9 genome engineering and ends-out gene-
614 targeting (Gratz et al., 2013; Huang et al., 2009, 2008). We used two guide RNAs that flank
615 *ppk1* (upstream gRNA: 5'-GTTCTTATATCTAGAGATGT-3', and downstream gRNA: 5'-
616 GTCAAGACTTGAAGAATACTG-3') and a donor template, which contained homology arms
617 surrounding an attP site and 3xP3-DsRed flanked by loxP sites. Candidate strains were
618 identified by DsRed expression in adult eyes, and the *ppk1* locus was analyzed by sequencing
619 genomic DNA from isogenized candidate strains. 3xP3-DsRed was then removed by crossing to
620 flies expressing Cre recombinase. A single strain with the desired replacement of *ppk1* with an
621 attP site was used to generate all knock-in alleles.

622

623 Constructs to create knock-in alleles were generated using standard molecular biology
624 techniques and Gibson Assembly to add molecular tags. Two plasmid backbones were used:
625 *pGE-attB-GMR* (Huang et al., 2009), which includes a *GMR-mini-white*$^{+}$ cassette to identify
626 knock-in alleles by red eye color in adults, and *pBSK-attB-3xP3* (this study), which includes a
627 *3xP3-DsRed* cassette to identify knock-in alleles by DsRed expression in adult eyes. *pBSK-*
628 *attB-3xP3* was generated by adding an *attB* site and *3xP3-DsRed* to *pBSK*. All the exogenous
629 sequences (e.g., the product of attB/attP recombination) knocked-into the endogenous *ppk1*
630 locus were the same regardless of which plasmid backbone was used. New *ppk1* alleles in the
631 *pGE-attB-GMR* vector were first subcloned into *pBSK*, modified, and then inserted into *pGE-*
632 *attB-GMR* using EcoRI and KpnI. New *ppk1* alleles in the *pBSK-attB-3xP3* plasmid were cloned
633 directly using Gibson Assembly (*pBSK-attB-3xP3-ppk*^{WT} was the starting plasmid for many of
634 the knock-in alleles). All constructs were verified by sequencing prior to injection. *attB-*
635 containing plasmids with *ppk1* knock-in alleles were injected into *ppk1*$^{attP\text{-}KO}$ embryos expressing
636 ΦC31 integrase (BestGene Inc., Chino Hills, CA). The *GMR-mini-w*$^{+}$ and *3xP3-DsRed* markers
637 were subsequently removed by crossing to flies expressing Cre recombinase.
638
639 The following alleles were generated in this study: First a wild-type knock-in allele (*ppk1*$^{WT\text{-}k'in}$)
640 was generated by cloning the part of the *ppk1* locus that was eliminated by the replacement
641 strategy (plasmid *pGE-attB-GMR-ppk1*^{WT}*)*. The resulting *ppk1*$^{WT\text{-}K'in}$ flies displayed no overt
642 phenotypes and restored the normal pattern of *ppk1* expression. sfGFP::Ppk1 and Ppk1::sfGFP
643 were created by adding one copy of sfGFP and a GGS(x4) linker at the N- or C-terminus,
644 respectively, of Ppk1 (plasmids *pGE-attB-GMR-sfGFP::ppk1* and *pGE-attB-GMR-ppk1::sfGFP*).
645 A similar approach was used to generate Ppk1::mCherry and sfGFP::Ppk1::mCherry (plasmids
646 *pBSK-attB-3xP3-ppk1::mCherry* and *pBSK-attB-3xP3-sfGFP::ppk1::mCherry*). Ppk1::sfGFP^{EC}-
647 Site 1 and Ppk1::sfGFP^{EC}-Site 2 were created by tagging Ppk1 with one copy of sfGFP at either
648 extracellular Site 1 (between Asn171 and Ile172) or Site 2 (between Gln204 and Leu205).
649 sfGFP was flanked on both sides by a GGS(x4) linker (plasmids *pBSK-attB-3xP3-*
650 *ppk1::sfGFP*^{EC}*-Site 1* and *pBSK-attB-3xP3-ppk1::sfGFP*^{EC}*-Site 2)*. Ppk1::GFP(11x3)^{EC} was
651 created by tagging Ppk1 with three copies of the split-GFP peptide GFP(11) at extracellular Site
652 1 (between Asn171 and Ile172). The three copies of GFP(11) were flanked on both sides by a
653 GGS(x4) linker (plasmid *pBSK-attB-3xP3-ppk1::GFP(11x3)*^{EC}). Ppk1::GFP(11x3)^{EC}::mCherry^{C-}
654 ^{term} was created by tagging Ppk1::GFP(11x3)^{EC} at the C-terminus with one copy of mCherry
655 connected by a GGS(x4) linker (plasmid *pBSK-attB-3xP3-ppk1::GFP(11x3)*^{EC}*::mCherry*$^{C\text{-}term}$).
656 Ppk1::GFP(11x7)$^{C\text{-}term}$ was created by tagging Ppk1 with seven copies of GFP(11) at the C-

657 terminus via a GGS(x4) linker (plasmid *pGE-attB-GMR-ppk1::GFP(11x7)*).
658 Ppk1::pHluorin^{EC}::mScarlet$^{C\text{-}term}$ and Ppk1::pHluorin^{EC}::mCherry$^{C\text{-}term}$ were created by adding one
659 copy of superecliptic pHluorin (synthesized as a gene block by GeneWiz, South Plainfield, NJ)
660 at extracellular Site 1 (between Asn171 and Ile172) and flanked on both sides by a GGS(x4)
661 linker and tagged at the C-terminus with either one copy of mScarlet-I (synthetic gene block
662 from GeneWiz) or one copy of mCherry connected with a GGS(x4) linker (plasmids *pGE-attB-*
663 *GMR-ppk1::pHluorin^{EC}::mScarlet$^{C\text{-}term}$* and *pBSK-attB-3xP3-ppk1::pHluorin^{EC}::mCherry$^{C\text{-}term}$*).
664
665 Generation of the UAS-secGFP(1-10) transgenic fly strain
666 The GFP(1-10) coding sequence, which was synthesized as a gBlock fragment (Integrated DNA
667 Technologies, Inc.), was PCR-amplified and cloned into the NheI/XbaI sites of *pIHEU-sfGFP-*
668 *LactC1C2* (Sapar et al., 2018). The resulting *pIHEU-secGFP(1-10)* construct contains a signal-
669 peptide sequence from Adipokinetic hormone fused in-frame before GFP(1-10). The construct
670 was inserted at the *attP^{VK00005}* site (injected by Rainbow Transgenic Flies, Inc).
671
672 Fixation and Immunohistochemistry
673 To visualize Ppk channel expression in larval fillets, wandering third instar larvae were washed
674 in 1X PBS (phosphate buffered saline, pH 7.4), dissected in PHEM buffer (80 mM PIPES pH
675 6.9, 25 mM HEPES pH 7.0, 7 mM $MgCl_2$, 1 mM EGTA) and fixed in 4% paraformaldehyde in 1X
676 PBS with 3.2% sucrose for 20 minutes. For the dissection, larvae were pinned onto a Sylgard
677 plate with their dorsal trachea facing down and were cut on their ventral side to preserve the
678 ddaC neurons. After fixation, the dissected fillets were washed 3 times with 1X PBS, quenched
679 with 50 mM NH_4Cl for 10 minutes, and blocked in blocking buffer composed of 2.5% bovine
680 serum albumin (BSA; catalog number A9647, Sigma), 0.25% fish-skin gelatin (FSG; catalog
681 number G7765, Sigma), 10 mM glycine, and 50 mM NH_4Cl for 3 hours at room temperature.
682 Fillets were incubated in primary antibody diluted in blocking buffer overnight at 4˚C. The next
683 day, fillets were washed in 1X PBS at room temperature (3 x 30 minutes) and incubated with
684 secondary antibody diluted in blocking buffer overnight at 4˚C. The next day, fillets were washed
685 in 1X PBS at room temperature (3 x 30 minutes) and mounted onto glass microscope slides
686 (Fisher Scientific, Selectfrost, 25x75x1.0 mm) with cover glass (Fisher Scientific 24x50-1.5)
687 using elvanol containing antifade (polyvinyl alcohol, Tris-HCl pH 8.5, glycerol and DABCO,
688 catalog number 11247100, Fisher Scientific, Hampton, NH). All wash and incubation steps were
689 performed on a nutator. To visualize membrane levels of Ppk1, a rabbit anti-Ppk1 antibody
690 (1:3000; gift of Yuh Nung Jan, UCSF) (Gorczyca et al., 2014) targeting an extracellular epitope

691 of Ppk1 was used without detergent in any wash or incubation steps. A fluorescently conjugated
692 secondary antibody was used: goat anti-rabbit-Dylight 633 (1:500; catalog #35563, Invitrogen).
693
694 To visualize Ppk expression in the ventral nerve cord, brains from wandering third instar larvae
695 were isolated from larval carcasses in 1x PBS. Following fixation (4% paraformaldehyde in 1X
696 PBS with 3.2% sucrose for 15 minutes), brains were washed (3 X 5 minutes) in 1x PBS and
697 mounted with the optic lobes facing down. The cover glass was stabilized with four small dots of
698 vacuum grease spacers in four corners of the slide.
699
700 To visualize Ppk1::sfGFP in young ddaC neurons, embryos were collected on grape plates for
701 several hours and then devitalized in a solution of 50% bleach and 50% H_2O for 2-3 minutes.
702 The eggshells were washed away by rinsing with H_2O and then placed in a tube containing
703 equal quantities of n-heptane and fixative (4% paraformaldehyde in 1X PBS) for 10 minutes.
704 Fixed embryos were washed with 1X PBS with 0.1% Triton X-100 (3 x 10 minutes) and then
705 probed for 2 hours with goat anti-HRP conjugated Alexa Fluor 647 (1:1000, or 0.5 mg/mL,
706 Jackson ImmunoResearch, West Grove, PA). The anti-HRP antibody recognizes a glycoprotein
707 epitope that is present throughout the fruit fly nervous system, enabling visualization of virtually
708 all neuronal membranes. Following incubation with the anti-HRP antibody, the embryos were
709 washed in 1X PBS with 0.1% Triton X-100 (3 x 30 minutes). Embryos were mounted in a
710 solution of 50% glycerol and 50% 1X PBS on glass microscope slides (Fisher Scientific,
711 Selectfrost, 25x75x1.0 mm) with cover glass (Global Scientific, 24x50 mm-1.5). All steps were
712 performed at room temperature.
713
714 Imaging
715 Imaging was performed on either an SP5 or Stellaris laser-scanning confocal microscope (Leica
716 Microsystems) with sensitive hybrid (HyD) and photomultiplier tube (PMT) detectors using
717 20×0.7 NA (SP5), 20×0.75 NA (Stellaris), and 40×1.3 NA (SP5 and Stellaris) oil-immersion
718 objectives. The dorsal class IV da neurons (ddaCs) in abdominal segments A2-A5 of control
719 and mutant larvae were imaged. For live imaging, individual larvae were placed into a small
720 drop of 50% glycerol:1X PBS solution that was flanked on both sides by strips of vacuum
721 grease spacers. The larva was then immobilized by pressing a cover glass on top of the
722 spacers. The larva was oriented with its dorsal trachea facing up and rolled gently to one side
723 for optimal positioning of the ddaC neurons. Fixed samples (larval fillets, VNCs) were imaged
724 using a 40×1.3 NA oil-immersion objective. Images were collected via z-stacks (1024x1024-

725 pixel resolution, 1 μm per z-step). Movies of Ppk1::sfGFP and Ppk1::mCherry dynamics were
726 collected in 120 h AEL larvae using a 40×1.3 NA oil-immersion objective at a resolution of 1024
727 x 256 pixels, zoom 2.5, and a rate of 2-1.35 frames per second, or 0.5-0.74 seconds per frame,
728 respectively, for a duration of 3 minutes. Movies of Ppk1::GFP(11)^{EC} in growing dendrite tips
729 were collected in 72 h AEL larvae using a 40×1.3 NA oil-immersion objective at a resolution of
730 1024 x 256 pixels, zoom 6, and a rate of 0.34 frames per second (2.942 seconds per frame) for
731 a duration of 3 minutes. For FRAP: First, a pre-bleach z-stack was obtained of the dendrite
732 region to be bleached, which was a secondary dendrite segment longer than 50 μm without
733 branch points, visible in a single z-plane, and within 150 μm of the cell body. A 50 μm circular
734 region of interest (ROI) was centered on the dendrite segment. Next, the Leica FRAP Wizard
735 was used to bleach the ROI: pre-bleach (10 frames; 0.739 sec/frame), bleach at 100% 488 laser
736 intensity (10 frames; 0.739 sec/frame), post-bleach (10 frames; 0.739 sec/frame). After
737 bleaching, z-stacks (z-step size of 0.5 μm) were captured at 1, 3, 5, 10, and 20 minutes post-
738 bleaching. For all experiments, the same imaging settings were used for control and
739 experimental conditions. Images and movies were subsequently analyzed using FIJI or
740 Metamorph.
741
742 Quantification of Ppk1 signal
743 Levels of Ppk1 were measured in FIJI using the following reporters: anti-Ppk1 antibody,
744 Ppk1::sfGFP, Ppk1::mCherry, and Ppk1::sfGFP(11x3)^{EC}::mCherry$^{C\text{-}term}$. First, maximum intensity
745 projections of z-stack images were generated. To quantify levels in dendrites, the fluorescence
746 intensity of three different dendrite branches was quantified by tracing 50-μm lines over
747 segments close to the cell body and averaging the signal intensity along each segment. The
748 average intensity of a 50-μm line traced over the background was subtracted from each dendrite
749 trace. Under non-permeabilizing conditions, anti-Ppk1 signal was weak surrounding the cell
750 body, and therefore dendrite traces initiated ~10-15 μm away from the cell body. An average
751 intensity for each neuron was quantified by averaging the intensities of the three dendrite
752 segments after subtracting the background signal. A similar protocol was used to determine the
753 fluorescence intensity of Ppk1::sfGFP in axons: a 50-μm line was traced over the axon close to
754 the cell body and the average intensity of a 50-μm line traced over the background was
755 subtracted.
756
757 To measure the extent of Ppk1::sfGFP signal in growing dendrites over time, z-stack images of
758 Ppk1::sfGFP and CD4::tdTomato taken at two time points 30 sec apart were aligned using the

759 bUnwarpJ plugin to generate a composite image representing the change in dendrite length and
760 fluorescent signal over time. Dendrite length was quantified based on the CD4::tdTomato signal,
761 and the percentage of dendrite that was Ppk1::sfGFP-positive was calculated.
762
763 Quantification of Ppk1::sfGFP and Ppk1::mCherry dynamics
764 Movies of Ppk1::sfGFP and Ppk1::mCherry dynamics were first stabilized in FIJI using the
765 Image Stabilizer plugin. Stabilized movies were opened in Metamorph (Molecular Devices, LLC,
766 San Jose, CA), and kymographs were generated by drawing 50-70 μm line segments along
767 dendrites and axons. Frequency was quantified by manually counting the number of motile and
768 stationary puncta (data were normalized to represent the number of puncta in 100 μm and 1
769 minute). To quantify motility, the tracks on each kymograph were manually divided into three
770 categories. Puncta that were motile for the duration of the movie were scored as mobile. Some
771 puncta were both motile and stationary; these puncta were scored as "both." Puncta that did not
772 move (defined as less than 1 μm) for the duration of the 3-minute movie were scored as
773 stationary. To quantify directionality, the tracks on the kymograph were manually scored as
774 anterograde (away from the cell body), retrograde (towards the cell body), or bidirectional
775 (anterograde and retrograde movement). To quantify velocity, tracks on the kymograph were
776 traced, and the corresponding data on time and distance were exported to Excel to calculate
777 velocity.
778
779 Quantification of dendrite morphology
780 Imaris software with Filament Tracer (version 9.7-9.8, Oxford Instruments) was used to quantify
781 dendrite length and the number of terminal tips. Neurons were analyzed in larvae that were
782 aged to 72 h AEL unless otherwise mentioned. To capture the entire ddaC dendritic arbor, z-
783 stacks (1024x1024-pixel resolution, 1 μm per z-step) of neurons expressing fluorescent
784 membrane markers were captured using a 20×0.7 NA (Leica SP5) 20×0.75 NA (Leica Stellaris)
785 oil-immersion objectives. Maximum intensity projections of the z-stack images were created in
786 FIJI, and neighboring neurons were cropped out using the freehand draw tool. These images
787 were then further processed in FIJI by applying a threshold to eliminate background signal. The
788 images were imported into Imaris, and Filament Tracer (BitPlane) with automatic detection was
789 used to quantify total dendrite length and the number of terminal tips. The largest and smallest
790 diameters of each neuron were manually measured to generate the dendrite start points and
791 seed points. The thresholds were manually adjusted for the start points and seed points in order
792 to cover the entire arbor and to reduce background points; seed points were manually added to

segments that were not automatically identified. The filament was edited to remove the axon segment and to correct misdrawn segments. Measurements generated in Imaris were exported to Excel for further analysis.

Quantification of FRAP

Analysis was performed in FIJI by creating maximum projections of the z-stacks from each time point. A line trace through the bleached region was drawn and the average intensity (arbitrary units; AU) of the center 10 μm was used to quantify the signal recovery over time. To account for general photobleaching, the signal intensity in the bleached 10 μm section was normalized by dividing by the average intensity (AU) of a 10 μm segment in a different secondary branch outside of the bleached region. Average intensity values were exported to Excel for further analysis. To calculate percent recovery of signal after photobleaching, the normalized average signal of the 10 μm branched region at 1, 3, 5, 10, and 20 minutes was divided by the initial signal from the pre-bleach z-stack.

Statistical Analysis

All data were blinded prior to analysis. Statistical analysis was performed in Excel and GraphPad Prism using a significance level of $p < 0.05$. Outliers were identified using Grubbs' test and removed. Data were analyzed for normality using the Shapiro-Wilk test. Normally distributed data were then analyzed for equal variance and significance using either an F-test and Student's unpaired t-test (two samples) or one-way ANOVA with post-hoc Tukey (multiple samples). Data sets that were not normally distributed were analyzed using Mann-Whitney U test (two samples) or Kruskal-Wallis test with post-hoc Dunn test for significance (multiple samples). Significance levels are represented as follows: not significant (ns), $p > 0.05$; *, $p = 0.05$-0.01; **, $p = 0.01$-0.001; ***, $p = 0.001$-0.0001; and ****, $p < 0.0001$. Data are presented as the mean ± standard error of the mean (SEM) unless otherwise noted. In the graphs, *n* represents a neuron unless otherwise indicated.

Acknowledgements

We thank Drs. Yuh Nung Jan (University of California, San Francisco), Hsiu-Hsiang Lee (National Taiwan University College of Medicine), Bing Ye (University of Michigan), the Bloomington Drosophila Stock Center (NIH P40OD018537), and the Vienna Drosophila Resource Center for fly strains and antibodies. We thank Dr. Anjon Audhya and Jennifer Peotter (University of Wisconsin-Madison) for assistance with the Imaris software. We thank members of the Wildonger lab for their feedback and suggestions on the project and manuscript; in particular, we thank Jessica Liang for her contributions to developing the FRAP protocol, Dena Johnson-Schlitz for technical assistance and advice, and Harriet Saunders for helpful guidance. We thank the Biochemistry Department and Dr. Aaron Hoskins (University of Wisconsin-Madison) for generously providing funding and space to support J.M.. This work is supported by NIH R01NS102385 (J.W.), R01NS099125 (C.H.), and generous funds from the University of Wisconsin-Madison (J.W.), the University of California, San Diego (J.W.), and Cornell University (C.H.).

Author Contributions

J.M. and J.W. conceived of the study. J.M. and I.M. conducted experiments and analyzed data. B.W. and C.H. conceived of the split-GFP approach to identify the membrane insertion of proteins and designed and generated the UAS-secreted-GFP(1-10) fly strain. J.M. and J.W. wrote the manuscript with input from all the authors.

847 **References**
848

849 Adams CM, Anderson MG, Motto DG, Price MP, Johnson WA, Welsh MJ. 1998. Ripped Pocket
850 and Pickpocket, Novel Drosophila DEG/ENaC Subunits Expressed in Early Development
851 and in Mechanosensory Neurons. *J Cell Biology* 140:143–152. doi:10.1083/jcb.140.1.143

852 Ainsley JA, Kim MJ, Wegman LJ, Pettus JM, Johnson WA. 2008. Sensory mechanisms
853 controlling the timing of larval developmental and behavioral transitions require the
854 Drosophila DEG/ENaC subunit, Pickpocket1. *Dev Biol* 322:46–55.
855 doi:10.1016/j.ydbio.2008.07.003

856 Ang AL, Taguchi T, Francis S, Fölsch H, Murrells LJ, Pypaert M, Warren G, Mellman I. 2004.
857 Recycling endosomes can serve as intermediates during transport from the Golgi to the
858 plasma membrane of MDCK cells. *J Cell Biology* 167:531–543. doi:10.1083/jcb.200408165

859 Arthur AL, Yang SZ, Abellaneda AM, Wildonger J. 2015. Dendrite arborization requires the
860 dynein cofactor NudE. *J Cell Sci* 128:2191–2201. doi:10.1242/jcs.170316

861 Banerjee S. 2006. Axonal Ensheathment and Septate Junction Formation in the Peripheral
862 Nervous System of Drosophila. *J Neurosci* 26:3319–3329. doi:10.1523/jneurosci.5383-
863 05.2006

864 Bianchi L. 2022. Ion Channels in Biophysics and Physiology. *Adv Exp Med Biol* 1349:165–192.
865 doi:10.1007/978-981-16-4254-8_9

866 Bianchi L, Gerstbrein B, Frøkjær-Jensen C, Royal DC, Mukherjee G, Royal MA, Xue J, Schafer
867 WR, Driscoll M. 2004. The neurotoxic MEC-4(d) DEG/ENaC sodium channel conducts
868 calcium: implications for necrosis initiation. *Nat Neurosci* 7:1337–1344. doi:10.1038/nn1347

869 Boscardin E, Alijevic O, Hummler E, Frateschi S, Kellenberger S. 2016. The function and
870 regulation of acid-sensing ion channels (ASICs) and the epithelial Na+ channel (ENaC):
871 IUPHAR Review 19. *Brit J Pharmacol* 173:2671–2701. doi:10.1111/bph.13533

872 Bourke AM, Bowen AB, Kennedy MJ. 2018. New approaches for solving old problems in
873 neuronal protein trafficking. *Mol Cell Neurosci*. doi:10.1016/j.mcn.2018.04.004

874 Bowen AB, Bourke AM, Hiester BG, Hanus C, Kennedy MJ. 2017. Golgi-independent secretory
875 trafficking through recycling endosomes in neuronal dendrites and spines. *Elife* 6:e27362.
876 doi:10.7554/elife.27362

877 Brown AL, Fernandez-Illescas SM, Liao Z, Goodman MB. 2007. Gain-of-Function Mutations in
878 the MEC-4 DEG/ENaC Sensory Mechanotransduction Channel Alter Gating and Drug
879 Blockade. *J Gen Physiology* 129:161–173. doi:10.1085/jgp.200609672

880 Butterworth MB, Edinger RS, Silvis MR, Gallo LI, Liang X, Apodaca G, Frizzell RA, Fizzell RA,
881 Johnson JP. 2012. Rab11b regulates the trafficking and recycling of the epithelial sodium
882 channel (ENaC). *Am J Physiol-renal* 302:F581–F590. doi:10.1152/ajprenal.00304.2011

883 Chen X, Gründer S. 2007. Permeating protons contribute to tachyphylaxis of the acid-sensing
884 ion channel (ASIC) 1a. *J Physiology* 579:657–670. doi:10.1113/jphysiol.2006.120733

885 Chudakov DM, Matz MV, Lukyanov S, Lukyanov KA. 2010. Fluorescent Proteins and Their
886 Applications in Imaging Living Cells and Tissues. *Physiol Rev* 90:1103–1163.
887 doi:10.1152/physrev.00038.2009

888 Coste B, Xiao B, Santos JS, Syeda R, Grandl J, Spencer KS, Kim SE, Schmidt M, Mathur J,
889 Dubin AE, Montal M, Patapoutian A. 2012. Piezos are pore-forming subunits of mechanically
890 activated channels. *Nature* 483:176–181. doi:10.1038/nature10812

891 Craig AM, Blackstone CD, Huganir RL, Banker G. 1993. The distribution of glutamate receptors
892 in cultured rat hippocampal neurons: Postsynaptic clustering of AMPA selective subunits.
893 *Neuron* 10:1055–1068. doi:10.1016/0896-6273(93)90054-u

894 Cresawn KO, Potter BA, Oztan A, Guerriero CJ, Ihrke G, Goldenring JR, Apodaca G, Weisz
895 OA. 2007. Differential involvement of endocytic compartments in the biosynthetic traffic of
896 apical proteins. *Embo J* 26:3737–3748. doi:10.1038/sj.emboj.7601813

897 Darboux I, Lingueglia E, Pauron D, Barbry P, Lazdunski M. 1998. A New Member of the
898 Amiloride-Sensitive Sodium Channel Family inDrosophila melanogasterPeripheral Nervous
899 System. *Biochem Bioph Res Co* 246:210–216. doi:10.1006/bbrc.1998.8183

900 Echeverri CJ, Paschal BM, Vaughan KT, Vallee RB. 1996. Molecular characterization of the 50-
901 kD subunit of dynactin reveals function for the complex in chromosome alignment and
902 spindle organization during mitosis. *J Cell Biology* 132:617–633. doi:10.1083/jcb.132.4.617

903 Ehlers MD, Fung ET, O'Brien RJ, Huganir RL. 1998. Splice Variant-Specific Interaction of the
904 NMDA Receptor Subunit NR1 with Neuronal Intermediate Filaments. *J Neurosci* 18:720–
905 730. doi:10.1523/jneurosci.18-02-00720.1998

906 Emoto K, He Y, Ye B, Grueber WB, Adler PN, Jan LY, Jan Y-N. 2004. Control of Dendritic
907 Branching and Tiling by the Tricornered-Kinase/Furry Signaling Pathway in Drosophila
908 Sensory Neurons. *Cell* 119:245–256. doi:10.1016/j.cell.2004.09.036

909 Freeman MR. 2015. Drosophila Central Nervous System Glia. *Csh Perspect Biol* 7:a020552.
910 doi:10.1101/cshperspect.a020552

911 Gardiol A, Racca C, Triller A. 1999. Dendritic and Postsynaptic Protein Synthetic Machinery. *J*
912 *Neurosci* 19:168–179. doi:10.1523/jneurosci.19-01-00168.1999

913 Gill I, Droubi S, Giovedi S, Fedder KN, Bury LAD, Bosco F, Sceniak MP, Benfenati F, Sabo SL.
914 2014. Presynaptic NMDA receptors – dynamics and distribution in developing axons in vitro
915 and in vivo. *J Cell Sci* 128:768–780. doi:10.1242/jcs.162362

916 Gorczyca DA, Younger S, Meltzer S, Kim SE, Cheng L, Song W, Lee HY, Jan LY, Jan YN.
917 2014. Identification of Ppk26, a DEG/ENaC Channel Functioning with Ppk1 in a Mutually
918 Dependent Manner to Guide Locomotion Behavior in Drosophila. *Cell Reports* 9:1446–1458.
919 doi:10.1016/j.celrep.2014.10.034

920 Gratz SJ, Cummings AM, Nguyen JN, Hamm DC, Donohue LK, Harrison MM, Wildonger J,
921 O'Connor-Giles KM. 2013. Genome Engineering of Drosophila with the CRISPR RNA-
922 Guided Cas9 Nuclease. *Genetics* 194:1029–1035. doi:10.1534/genetics.113.152710

923 Grueber WB, Jan LY, Jan YN. 2002. Tiling of the Drosophila epidermis by multidendritic sensory
924 neurons. *Development* 129:2867–78.

925 Grueber WB, Ye B, Moore AW, Jan LY, Jan YN. 2003. Dendrites of Distinct Classes of
926 Drosophila Sensory Neurons Show Different Capacities for Homotypic Repulsion. *Curr Biol*
927 13:618–626. doi:10.1016/s0960-9822(03)00207-0

928 Guo Y, Wang Y, Wang Q, Wang Z. 2014. The Role of PPK26 in Drosophila Larval Mechanical
929 Nociception. *Cell Reports* 9:1183–1190. doi:10.1016/j.celrep.2014.10.020

930 Hall DH, Treinin M. 2011. How does morphology relate to function in sensory arbors? *Trends*
931 *Neurosci* 34:443–451. doi:10.1016/j.tins.2011.07.004

932 Han C, Wang D, Soba P, Zhu S, Lin X, Jan LY, Jan Y-N. 2012. Integrins Regulate Repulsion-
933 Mediated Dendritic Patterning of Drosophila Sensory Neurons by Restricting Dendrites in a
934 2D Space. *Neuron* 73:64–78. doi:10.1016/j.neuron.2011.10.036

935 Hausser A, Schlett K. 2017. Coordination of AMPA receptor trafficking by Rab GTPases. *Small*
936 *Gtpases* 10:419–432. doi:10.1080/21541248.2017.1337546

937 He J, Li B, Han S, Zhang Y, Liu K, Yi S, Liu Y, Xiu M. 2022. Drosophila as a Model to Study the
938 Mechanism of Nociception. *Front Physiol* 13:854124. doi:10.3389/fphys.2022.854124

939 Herkert M, Röttger S, Becker C. 1998. The NMDA receptor subunit NR2B of neonatal rat brain:
940 complex formation and enrichment in axonal growth cones. *Eur J Neurosci* 10:1553–1562.
941 doi:10.1046/j.1460-9568.1998.00164.x

942 Horton AC, Ehlers MD. 2003. Dual Modes of Endoplasmic Reticulum-to-Golgi Transport in
943 Dendrites Revealed by Live-Cell Imaging. *J Neurosci* 23:6188–6199.
944 doi:10.1523/jneurosci.23-15-06188.2003

945 Hu C, Kanellopoulos AK, Richter M, Petersen M, Konietzny A, Tenedini F, Hoyer N, Cheng L,
946 Poon CLC, Harvey KF, Windhorst S, Parrish JZ, Mikhaylova M, Bagni C, Anda FC de, Soba
947 P. 2020. Conserved Tao kinase activity regulates dendritic arborization, cytoskeletal
948 dynamics and sensory function in Drosophila. *J Neurosci* 1846–19.
949 doi:10.1523/jneurosci.1846-19.2020

950 Huang J, Zhou W, Dong W, Watson AM, Hong Y. 2009. Directed, efficient, and versatile
951 modifications of the Drosophila genome by genomic engineering. *Proc Natl Acad Sci*
952 106:8284–8289. doi:10.1073/pnas.0900641106

953 Huang J, Zhou W, Watson AM, Jan Y-N, Hong Y. 2008. Efficient Ends-Out Gene Targeting In
954 Drosophila. *Genetics* 180:703–707. doi:10.1534/genetics.108.090563

955 Hwang RY, Zhong L, Xu Y, Johnson T, Zhang F, Deisseroth K, Tracey WD. 2007. Nociceptive
956 Neurons Protect Drosophila Larvae from Parasitoid Wasps. *Curr Biol* 17:2105–2116.
957 doi:10.1016/j.cub.2007.11.029

958 Jan Y-N, Jan LY. 2010. Branching out: mechanisms of dendritic arborization. *Nat Rev Neurosci*
959 11:316–328. doi:10.1038/nrn2836

960 Jasti J, Furukawa H, Gonzales EB, Gouaux E. 2007. Structure of acid-sensing ion channel 1 at
961 1.9 Å resolution and low pH. *Nature* 449:316–323. doi:10.1038/nature06163

962 Jaszczak JS, DeVault L, Jan LY, Jan YN. 2022. Steroid hormone signaling activates thermal
963 nociception during Drosophila peripheral nervous system development. *Elife* 11:e76464.
964 doi:10.7554/elife.76464

965 Jegla T, Nguyen MM, Feng C, Goetschius DJ, Luna E, Rossum DB van, Kamel B, Pisupati A,
966 Milner ES, Rolls MM. 2016. Bilaterian Giant Ankyrins Have a Common Evolutionary Origin
967 and Play a Conserved Role in Patterning the Axon Initial Segment. *Plos Genet* 12:e1006457.
968 doi:10.1371/journal.pgen.1006457

969 Ji H, Sapar ML, Sarkar A, Wang B, Han C. 2022. Phagocytosis and self-destruction break down
970 dendrites of Drosophila sensory neurons at distinct steps of Wallerian degeneration. *Proc*
971 *Natl Acad Sci* 119:e2111818119. doi:10.1073/pnas.2111818119

972 Kamiyama R, Banzai K, Liu P, Marar A, Tamura R, Jiang F, Fitch MA, Xie J, Kamiyama D.
973 2021. Cell-type–specific, multicolor labeling of endogenous proteins with split fluorescent
974 protein tags in Drosophila. *Proc National Acad Sci* 118:e2024690118.
975 doi:10.1073/pnas.2024690118

976 Karpushev AV, Levchenko V, Pavlov TS, Lam V, Vinnakota KC, Vandewalle A, Wakatsuki T,
977 Staruschenko A. 2008. Regulation of ENaC expression at the cell surface by Rab11.
978 *Biochem Bioph Res Co* 377:521–525. doi:10.1016/j.bbrc.2008.10.014

979 Kellenberger S, Schild L. 2002. Epithelial Sodium Channel/Degenerin Family of Ion Channels: A
980 Variety of Functions for a Shared Structure. *Physiol Rev* 82:735–767.
981 doi:10.1152/physrev.00007.2002

982 Kerstein PC, Nichol RH, Gomez TM. 2015. Mechanochemical regulation of growth cone motility.
983 *Front Cell Neurosci* 9:244. doi:10.3389/fncel.2015.00244

984 Kim SE, Coste B, Chadha A, Cook B, Patapoutian A. 2012. The role of Drosophila Piezo in
985 mechanical nociception. *Nature* 483:209. doi:10.1038/nature10801

986 Krämer R, Rode S, Rumpf S. 2019. Rab11 is required for neurite pruning and developmental
987 membrane protein degradation in Drosophila sensory neurons. *Dev Biol* 451:68–78.
988 doi:10.1016/j.ydbio.2019.03.003

989 Leterrier C. 2018. The Axon Initial Segment: An Updated Viewpoint. *J Neurosci* 38:2135–2145.
990 doi:10.1523/jneurosci.1922-17.2018

991 Lin T, Kao H-H, Chou C-H, Chou C-Y, Liao Y-C, Lee H-H. 2020. Rab11 activation by Ik2 kinase
992 is required for dendrite pruning in Drosophila sensory neurons. *Plos Genet* 16:e1008626.
993 doi:10.1371/journal.pgen.1008626

994 Lin W-Y, Williams C, Yan C, Koledachkina T, Luedke K, Dalton J, Bloomsburg S, Morrison N,
995 Duncan KE, Kim CC, Parrish JZ. 2015. The SLC36 transporter Pathetic is required for
996 extreme dendrite growth in Drosophila sensory neurons. *Gene Dev* 29:1120–1135.
997 doi:10.1101/gad.259119.115

998 Liu X, Liu C, Ye J, Zhang S, Wang K, Su R. 2020. Distribution of Acid Sensing Ion Channels in
999 Axonal Growth Cones and Presynaptic Membrane of Cultured Hippocampal Neurons. *Front*
1000 *Cell Neurosci* 14:205. doi:10.3389/fncel.2020.00205

1001 Lock JG, Stow JL. 2005. Rab11 in Recycling Endosomes Regulates the Sorting and Basolateral
1002 Transport of E-Cadherin. *Mol Biol Cell* 16:1744–1755. doi:10.1091/mbc.e04-10-0867

1003 Lumpkin EA, Caterina MJ. 2007. Mechanisms of sensory transduction in the skin. *Nature*
1004 445:858–865. doi:10.1038/nature05662

1005 Mauthner SE, Hwang RY, Lewis AH, Xiao Q, Tsubouchi A, Wang Y, Honjo K, Skene JHP,
1006 Grandl J, Tracey WD. 2014. Balboa Binds to Pickpocket In Vivo and Is Required for
1007 Mechanical Nociception in Drosophila Larvae. *Curr Biol* 24:2920–2925.
1008 doi:10.1016/j.cub.2014.10.038

1009 Miesenböck G, Angelis DAD, Rothman JE. 1998. Visualizing secretion and synaptic
1010 transmission with pH-sensitive green fluorescent proteins. *Nature* 394:192–195.
1011 doi:10.1038/28190

1012 Ou Y, Chwalla B, Landgraf M, Meyel DJ van. 2008. Identification of genes influencing dendrite
1013 morphogenesis in developing peripheral sensory and central motor neurons. *Neural Dev*
1014 3:16. doi:10.1186/1749-8104-3-16

1015 Papoulas O, Hays TS, Sisson JC. 2004. The golgin Lava lamp mediates dynein-based Golgi
1016 movements during Drosophila cellularization. *Nat Cell Biol* 7:612–618. doi:10.1038/ncb1264

1017 Parrish JZ, Xu P, Kim CC, Jan LY, Jan YN. 2009. The microRNA bantam Functions in Epithelial
1018 Cells to Regulate Scaling Growth of Dendrite Arbors in Drosophila Sensory Neurons. *Neuron*
1019 63:788–802. doi:10.1016/j.neuron.2009.08.006

1020 Poe AR, Wang B, Sapar ML, Ji H, Li K, Onabajo T, Fazliyeva R, Gibbs M, Qiu Y, Hu Y, Han C.
1021 2018. Robust CRISPR/Cas9-Mediated Tissue Specific Mutagenesis Reveals Gene
1022 Redundancy and Perdurance in Drosophila. *Genetics* 211:genetics.301736.2018.
1023 doi:10.1534/genetics.118.301736

1024 Rao A, Kim E, Sheng M, Craig AM. 1998. Heterogeneity in the Molecular Composition of
1025 Excitatory Postsynaptic Sites during Development of Hippocampal Neurons in Culture. *J*
1026 *Neurosci* 18:1217–1229. doi:10.1523/jneurosci.18-04-01217.1998

1027 Rolls MM. 2011. Neuronal polarity in Drosophila: Sorting out axons and dendrites. *Dev*
1028 *Neurobiol* 71:419–429. doi:10.1002/dneu.20836

1029 Rui M, Bu S, Chew LY, Wang Q, Yu F. 2020. The membrane protein Raw regulates dendrite
1030 pruning via the secretory pathway. *Development* 147:dev191155. doi:10.1242/dev.191155

1031 Sapar ML, Ji H, Wang B, Poe AR, Dubey K, Ren X, Ni J-Q, Han C. 2018. Phosphatidylserine
1032 Externalization Results from and Causes Neurite Degeneration in Drosophila. *Cell Reports*
1033 24:2273–2286. doi:10.1016/j.celrep.2018.07.095

1034 Satoh D, Sato D, Tsuyama T, Saito M, Ohkura H, Rolls MM, Ishikawa F, Uemura T. 2008.
1035 Spatial control of branching within dendritic arbors by dynein-dependent transport of Rab5-
1036 endosomes. *Nat Cell Biol* 10:1164–1171. doi:10.1038/ncb1776

1037 Schenk U, Verderio C, Benfenati F, Matteoli M. 2003. Regulated delivery of AMPA receptor
1038 subunits to the presynaptic membrane. *Embo J* 22:558–568. doi:10.1093/emboj/cdg059

1039 Schroer TA. 2004. DYNACTIN. *Annu Rev Cell Dev Biology* 20:759–779.
1040 doi:10.1146/annurev.cellbio.20.012103.094623

1041 Singhania A, Grueber WB. 2014. Development of the embryonic and larval peripheral nervous
1042 system of Drosophila. *Wiley Interdiscip Rev Dev Biology* 3:193–210. doi:10.1002/wdev.135

1043 Sisson JC, Field C, Ventura R, Royou A, Sullivan W. 2000. Lava Lamp, a Novel Peripheral
1044 Golgi Protein, Is Required for Drosophila melanogaster Cellularization. *J Cell Biology*
1045 151:905–918. doi:10.1083/jcb.151.4.905

1046 Stork T, Engelen D, Krudewig A, Silies M, Bainton RJ, Klambt C. 2008. Organization and
1047 Function of the Blood Brain Barrier in Drosophila. *J Neurosci* 28:587–597.
1048 doi:10.1523/jneurosci.4367-07.2008

1049 Suh JM, Gao X, McKay J, McKay R, Salo Z, Graff JM. 2006. Hedgehog signaling plays a
1050 conserved role in inhibiting fat formation. *Cell Metab* 3:25–34.
1051 doi:10.1016/j.cmet.2005.11.012

1052 Tao L, Coakley S, Shi R, Shen K. 2022. Dendrites use mechanosensitive channels to proofread
1053 ligand-mediated guidance during morphogenesis. *Biorxiv* 2022.02.28.482179.
1054 doi:10.1101/2022.02.28.482179

1055 Tracey WD, Wilson RI, Laurent G, Benzer S. 2003. painless, a Drosophila Gene Essential for
1056 Nociception. *Cell* 113:261–273. doi:10.1016/s0092-8674(03)00272-1

1057 Wainman A, Creque J, Williams B, Williams EV, Bonaccorsi S, Gatti M, Goldberg ML. 2009.
1058 Roles of the Drosophila NudE protein in kinetochore function and centrosome migration. *J*
1059 *Cell Sci* 122:1747–1758. doi:10.1242/jcs.041798

1060 Wang PY, Petralia RS, Wang Y-X, Wenthold RJ, Brenowitz SD. 2011. Functional NMDA
1061 Receptors at Axonal Growth Cones of Young Hippocampal Neurons. *J Neurosci* 31:9289–
1062 9297. doi:10.1523/jneurosci.5639-10.2011

1063 Ware AW, Rasulov SR, Cheung TT, Lott JS, McDonald FJ. 2020. Membrane trafficking
1064 pathways regulating the epithelial Na+ channel. *Am J Physiol-renal* 318:F1–F13.
1065 doi:10.1152/ajprenal.00277.2019

1066 Winckler B, Forscher P, Mellman I. 1999. A diffusion barrier maintains distribution of membrane
1067 proteins in polarized neurons. *Nature* 397:698–701. doi:10.1038/17806

1068 Wong ROL, Ghosh A. 2002. Activity-dependent regulation of dendritic growth and patterning.
1069 *Nat Rev Neurosci* 3:803–812. doi:10.1038/nrn941

1070 Xiang Y, Yuan Q, Vogt N, Looger LL, Jan LY, Jan YN. 2010. Light-avoidance-mediating
1071 photoreceptors tile the Drosophila larval body wall. *Nature* 468:921–926.
1072 doi:10.1038/nature09576

1073 Yang SZ, Wildonger J. 2020. Golgi Outposts Locally Regulate Microtubule Orientation in
1074 Neurons but Are Not Required for the Overall Polarity of the Dendritic Cytoskeleton.
1075 *Genetics* 215:genetics.302979.2019. doi:10.1534/genetics.119.302979

1076 Ye B, Zhang Y, Song W, Younger SH, Jan LY, Jan YN. 2007. Growing Dendrites and Axons
1077 Differ in Their Reliance on the Secretory Pathway. *Cell* 130:717–729.
1078 doi:10.1016/j.cell.2007.06.032

1079 Younger MA, Müller M, Tong A, Pym EC, Davis GW. 2013. A Presynaptic ENaC Channel
1080 Drives Homeostatic Plasticity. *Neuron* 79:1183–1196. doi:10.1016/j.neuron.2013.06.048

1081 Zelle KM, Lu B, Pyfrom SC, Ben-Shahar Y. 2013. The Genetic Architecture of
1082 Degenerin/Epithelial Sodium Channels in Drosophila. *G3 Genes Genomes Genetics* 3:441–
1083 450. doi:10.1534/g3.112.005272

1084 Zhang J, Schulze KL, Hiesinger PR, Suyama K, Wang S, Fish M, Acar M, Hoskins RA, Bellen
1085 HJ, Scott MP. 2007. Thirty-One Flavors of Drosophila Rab Proteins. *Genetics* 176:1307–
1086 1322. doi:10.1534/genetics.106.066761

1087 Zheng Y, Wildonger J, Ye B, Zhang Y, Kita A, Younger SH, Zimmerman S, Jan LY, Jan YN.
1088 2008. Dynein is required for polarized dendritic transport and uniform microtubule orientation
1089 in axons. *Nat Cell Biol* 10:1172–1180. doi:10.1038/ncb1777

1090 Zhong L, Hwang RY, Tracey WD. 2010. Pickpocket Is a DEG/ENaC Protein Required for
1091 Mechanical Nociception in Drosophila Larvae. *Curr Biol* 20:429–434.
1092 doi:10.1016/j.cub.2009.12.057

1093 Zhou W, Chang J, Wang X, Savelieff MG, Zhao Y, Ke S, Ye B. 2014. GM130 Is Required for
1094 Compartmental Organization of Dendritic Golgi Outposts. *Curr Biol* 24:1227–1233.
1095 doi:10.1016/j.cub.2014.04.008

1096 Ziegler AB, Thiele C, Tenedini F, Richard M, Leyendecker P, Hoermann A, Soba P, Tavosanis
1097 G. 2017. Cell-Autonomous Control of Neuronal Dendrite Expansion via the Fatty Acid
1098 Synthesis Regulator SREBP. *Cell Reports* 21:3346–3353. doi:10.1016/j.celrep.2017.11.069

1099 **Figure Legends**

1100 **Figure 1. Endogenously tagged Ppk1 is enriched in dendrites but also localizes to axons.**

1101

1102 Images of ddaC neurons and their axon terminals in live 3rd instar larvae (B, D-F) and fixed
1103 ventral nerve cords (VNCs) (C, F). Dashed-outline boxes: Individual 1-µm thick z-plane zoomed-
1104 in views of dendrites and axons; a line indicates the position at which an intensity profile plot
1105 was generated (B, D).

1106

1107 **(A)** Cartoon illustrating the CRISPR-Cas9-engineered *ppk1* locus in which endogenous *ppk1*
1108 was replaced with an attP "docking" site for reliable, rapid knock-in of new *ppk1* alleles.

1109

1110 **(B, C)** Representative images of Ppk1::sfGFP in the cell body, dendrites, and axon (B) and axon
1111 terminals in the VNC (C). CD4::tdTomato marks the axon terminals of the class IV neurons in
1112 the VNC (C). Scale bars, 50 µm (B), 10 µm (C), and 5 µm (dashed-outline boxes, B).

1113

1114 **(D)** Representative image of Ppk1::mCherry. Scale bars, 50 µm and 5 µm (dashed-outline
1115 boxes).

1116

1117 **(E)** Representative kymographs and quantification of Ppk1::mCherry puncta in dendrites and
1118 axons. Quantification, Ppk1::mCherry puncta density: Mann-Whitney test ($p<0.0001$); dendrites
1119 (16 dendrite segments, 12 larvae) v. axons (12 axon segments, 9 larvae). In the graph, each
1120 data point represents a dendrite or axon segment. Quantification, Ppk1::mCherry puncta motility
1121 and directionality: dendrites (16 dendrite segments, 12 larvae) and axons (12 axon segments, 9
1122 larvae). Quantification, Ppk1::mCherry puncta velocity: Student's unpaired t-test ($p=0.8786$);
1123 dendrites (15 dendrite segments, 11 larvae) v. axons (12 axon segments, 9 larvae). In the
1124 graph, each data point represents the average velocity of Ppk1::mCherry puncta in a dendrite or
1125 axon segment. Data are plotted as mean ± SEM. n.s.=not significant ($p>0.05$) and ****$p<0.0001$.

1126

1127 **(F)** Representative images of dual-tagged sfGFP::Ppk1::mCherry in dendrites, cell body and
1128 axon (top and middle), and axon terminal in the VNC (bottom). Scale bars, 50 µm (top), 5 µm
1129 (middle), 10 µm (bottom).

1130

1131 **(G)** Representative images of the cell body and proximal dendrites of Ppk1::sfGFP,
1132 Ppk1::mCherry, and sfGFP::Ppk1::mCherry. Scale bar, 10 µm.

1133 **Figure 1 – Supplement 1. Effects of tagging endogenous Ppk1 on Ppk1 levels.**

1134

1135 Representative images and quantification of membrane-expressed Ppk1, recognized by anti-
1136 Ppk1 antibodies (top) and sfGFP-tagged Ppk1 (bottom) in w^{1118} control (12 larvae, 36 neurons),
1137 heterozygous N-terminally tagged Ppk1 (sfGFP::Ppk1) (11 larvae, 33 neurons), and
1138 heterozygous C-terminally tagged Ppk1 (Ppk1::sfGFP) (11 larvae, 33 neurons). Quantification,
1139 Ppk1 membrane levels: One-way ANOVA with post-hoc Tukey: w^{1118} v. *sfGFP::Ppk1*
1140 (p=0.2570), w^{1118} v. *Ppk1::sfGFP* (p=0.9097), *Ppk1::sfGFP* v. *sfGFP::Ppk1* (p=0.4802).
1141 Quantification, sfGFP-tagged Ppk1: Student's unpaired t-test (p=0.1707). In the graphs, each
1142 data point represents the average signal intensity per larva (2-3 neurons per larva). Data are
1143 plotted as mean ± SEM. n.s.=not significant (p>0.05). AU: arbitrary units. Scale bar, 50 μm.

1144 **Figure 2. Membrane localization of Ppk1 visualized in live larvae with the secreted split-**
1145 **GFP system.**
1146
1147 Images of ddaC neurons in live 3rd instar larvae (B-D) and fixed ventral nerve cords (VNCs) (E).
1148 Dashed-outline boxes: zoomed-in views of dendrite branches (B, C) and cell bodies (D) from the
1149 control neuron shown in panel B.
1150
1151 **(A)** Cartoon of secreted-split-GFP approach to label Ppk1 when it is inserted into the neuronal
1152 membrane. Secreted GFP(1-10) [secGFP(1-10)] is expressed by the fat bodies, which secrete
1153 secGFP(1-10) into the hemolymph that circulates throughout the larva. When secGFP(1-10)
1154 encounters and binds GFP(11) incorporated into an extracellular loop of ppk1, GFP is
1155 reconstituted and fluoresces.
1156
1157 **(B-D)** Representative images of GFP and mCherry fluorescence in neurons expressing either
1158 Ppk1 dual-tagged with 3 copies of GFP(11) extracellularly (EC) and mCherry at the C-terminus
1159 [Ppk1::GFP(11x3)^{EC}::mCherry$^{C\text{-}term}$] (B-D) or a control construct comprised of the single-pass
1160 transmembrane protein CD4 tagged extracellularly with one copy of GFP(11) and intracellularly
1161 with tdTomato [GFP(11)^{EC}::CD4::tdTomato] (D). UAS-secGFP(1-10) expression was driven in
1162 the fat bodies by DcG-Gal4. GFP fluorescence reveals that ppk1 is present in the neuronal
1163 membrane of the dendrites (B, C) and cell body (B, D) but not the axon, even though mCherry
1164 reveals that Ppk1 is present in axons (B, D). In contrast, GFP(11)^{EC}::CD4::tdTomato displays
1165 reconstituted GFP signal in both the cell body and the axon (D). Loss of *ppk26* (Δppk26:
1166 *ppk26*$^{\Delta 11/\Delta 11}$) results in an absence of GFP fluorescence from Ppk1::GFP(11x3)^{EC}::mCherry$^{C\text{-}term}$
1167 (B). Panel C shows a single 1-µm thick z-plane image of a dendrite segment from the neuron in
1168 panel B; the line indicates the position at which the intensity profile plot was generated. AU:
1169 arbitrary units. Solid arrowheads: cell body (B); open arrowheads: cell body-axon boundary (D).
1170 Scale bars, 50 µm (B, solid-outline boxes), 10 µm (B, dashed-outline boxes; D), and 5 µm (C).
1171
1172 **(E)** Representative images of Ppk1::GFP(11x3)^{EC}::mCherry$^{C\text{-}term}$ in axon terminals in the VNC.
1173 Scale bars, 10 µm. Solid arrowheads: mCherry signal in the axons terminating in the VNC.

1174 **Figure 2 – Supplement 1. Endogenous Ppk1 tagged with sfGFP at two different sites in an**
1175 **extracellular loop.**
1176
1177 Representative images of ddaC neurons expressing Ppk1 tagged with one copy of sfGFP at two
1178 different extracellular (EC) sites, Site 1 (between Asn171 and Ile172) and Site 2 (between
1179 Gln204 and Leu205). Ppk1 tagged with sfGFP at Site 1 showed similar fluorescent signal as
1180 Ppk1 tagged with sfGFP at the N- or C- terminus; thus, Site 1 was used for the insertion of
1181 additional tags [superecliptic pHluorin and GFP(11)]. Site 2 is located six amino acids
1182 downstream of the position at which a haemagglutinin (HA) tag was inserted (between F147
1183 and K148) in rASIC1a (Chen and Gründer, 2007). On the right, a cartoon shows the crystal
1184 structure of an individual cASIC1 subunit; ASIC is comprised of three subunits (PDB: 2QTS;
1185 Jasti et al., 2007). The sites that correspond to where sfGFP was inserted in fly ppk1 are
1186 indicated (the fly amino acid sequences are shown). The locations of Site 1 and Site 2 were
1187 predicted by aligning the amino acid sequences of ppk1 and cASIC1.

1188 **Figure 2 – Supplement 2. Ppk1 tagged extracellularly with pHluorin.**

1189

1190 **(A)** Representative image of a ddaC neuron expressing Ppk1 tagged extracellularly (EC) with
1191 one copy of pHluorin at Site 1 and with mCherry at the C-terminus (Ppk1::pHluorin^{EC}::mCherry^{C-}
1192 ^{term}). The neuron is heterozygous for *Ppk1::pHluorin^{EC}::mCherry^{C-term}*. Scale bar, 50 μm.

1193

1194 **(B)** Representative images of ddaC neurons expressing Ppk1 tagged extracellularly with one
1195 copy of pHluorin at Site 1 and with mScarlet at the C-terminus (Ppk1::pHluorin^{EC}::mScarlet^{C-term})
1196 in *w^{1118}* control and *ppk26* null (Δppk26: *ppk26$^{Δ11/Δ11}$*) larvae. The neurons are homozygous for
1197 *Ppk1::pHluorin^{EC}::mScarlet^{C-term}*. Scale bar, 50 μm.

1198 **Figure 2 – Supplement 3. Characterization of a split-GFP approach to label membrane-**
1199 **expressed Ppk1.**
1200
1201 **(A)** There is no GFP fluorescence in animals expressing *DcG-Gal4* and *UAS-secGFP(1-10)* in
1202 the absence of a protein tagged with GFP(11).
1203
1204 **(B)** Without the *DcG-Gal4* driver, there is no GFP fluorescence in animals expressing *UAS-*
1205 *secGFP(1-10)* and *Ppk1::GFP(11x3)^{EC}::mCherry$^{C\text{-}term}$*.
1206
1207 **(C)** There is no GFP fluorescence from Ppk1::GFP(11x3)^{EC}::mCherry$^{C\text{-}term}$ when GFP(1-10) is
1208 expressed in ddaC neurons by *ppk-Gal4*. The GFP(11x3) tag is positioned in an extracellular
1209 loop of Ppk1 and does not encounter cytosolic GFP(1-10). The red channel contains both the
1210 mCherry tag on the C-terminus of Ppk1 and a CD4::tdTomato membrane marker (*ppk-*
1211 *CD4::tdTomato*).
1212
1213 **(D)** There is GFP signal from Ppk1 tagged at the C-terminus with GFP(11) [Ppk1::GFP(11x7)$^{C-}$
1214 ^{term}] when GFP(1-10) is expressed in ddaC neurons by *ppk-Gal4*. The GFP(11x7) tag is on the
1215 intracellular Ppk1 C-terminus, which enables GFP(11x7) to interact with cytosolic GFP(1-10).
1216
1217 Scale bar, 50 μm.

1218 **Figure 2 – Supplement 4. Characterization of conditions that allow for GFP fluorescence**
1219 **of GFP(11)^{EC}::CD4::tdTomato.**
1220
1221 **(A)** There is no GFP fluorescence from GFP(11)^{EC}::CD4::tdTomato in the absence of
1222 secGFP(1-10).
1223
1224 **(B)** There is no GFP fluorescence from GFP(11)^{EC}::CD4::tdTomato when GFP(1-10) is
1225 expressed in ddaC neurons by *ppk-Gal4*. The GFP(11) tag is positioned at the extracellular N-
1226 terminus of CD4 and does not encounter cytosolic GFP(1-10).
1227
1228 **(C)** There is GFP signal from GFP(11)^{EC}::CD4::tdTomato when *DcG-Gal4* drives expression of
1229 *UAS-secGFP(1-10)*. A zoomed-in view of the cell body and proximal axon of this neuron is
1230 shown in Figure 2D.
1231
1232 *GFP(11)^{EC}::CD4::tdTomato* is expressed in the class IV neurons under the control of the *ppk*
1233 enhancer (*ppk-GFP(11)^{EC}::CD4::tdTomato)*. Blue arrowheads point to the cell body. Scale bar,
1234 50 µm.

1235 **Figure 3. Ppk1 is present in actively growing dendrites but the Pickpocket channel is not**
1236 **required for dendrite growth.**
1237
1238 Images of ddaC neurons in fixed embryos (A) and live 3rd instar larvae (B-E).
1239
1240 **(A)** Ppk1::sfGFP in the cell body and axon of a ddaC neuron in a late-stage embryo. The ddaC
1241 neuron is part of a cluster of sensory neurons, which are marked by anti-HRP. Arrowheads point
1242 to Ppk1::sfGFP in nascent dendrites. Scale bar, 10 μm.
1243
1244 **(B)** Quantification of the distribution of Ppk1::sfGFP in growing dendrite branches over 30
1245 minutes. Top graph: In growing branches, Ppk1::sfGFP signal was quantified as a percentage of
1246 the branch length marked by CD4::tdTomato (de novo: 11 branches, 4 neurons; existing: 18
1247 branches, 5 neurons). Ppk1::sfGFP was present along the entire length of the branch. Bottom
1248 graph: In 30 minutes, both newly formed and existing branches grew equivalent lengths (de
1249 novo: 11 branches, 4 neurons; existing: 19 branches, 5 neurons).
1250
1251 **(C)** Still images (top) and kymographs (bottom) from a 3-minute movie of GFP fluorescence
1252 from Ppk1::GFP(11x3)^{EC} in a growing dendrite tip marked by CD4::tdTomato. Arrowheads point
1253 to initial and final locations of dendrite growth. Genotype: *Ppk1::GFP(11x3)^{EC}/DcG-Gal4; UAS-*
1254 *secGFP(1-10)/ppk-CD4::tdTomato*. Scale bars, 3 μm.
1255
1256 **(D)** Representative images and quantification of FRAP of GFP in neurons expressing
1257 Ppk1::GFP(11x3)^{EC}::mCherry$^{C\text{-}term}$ and GFP(11)^{EC}::CD4::tdTomato (both genotypes: 8 neurons,
1258 8 larvae). Quantification, percent recovery: Student's unpaired t-test, 1 min (p=0.5417), 3 min
1259 (p=0.0108), 5 min (p=0.0064); 10 min (p<0.0001); 20 min (p=0.0021). In the image montage,
1260 dashed lines represent the bleached region, which was within 50-150 μm of the cell body. The
1261 GFP signal in a 10 μm section centered in the bleached region was quantified at each of the
1262 indicated time points. Scale bar, 10 μm.
1263
1264 **(E)** Representative images and quantification of control neurons (*w^{1118}*; 12 neurons, 5 larvae)
1265 and neurons lacking both Ppk1 and Ppk26 [Δppk1 (*ppk1$^{attP\text{-}KO/attP\text{-}KO}$*); Δppk26 (*ppk26$^{\Delta 11/\Delta 11}$*); 8
1266 neurons, 4 larvae]. Quantification, dendrite length: Student's unpaired t-test (p=0.9783).
1267 Quantification, dendrite tip number: Student's unpaired t-test (p=0.2592). The neuronal
1268 membrane is marked by CD4::GFP (*ppk-CD4::GFP*). Scale bar, 100 μm.

1269

1270 In the graphs, each data point represents either a dendrite branch (B) or a neuron (E), and data
1271 are plotted as mean ± SEM. n.s.=not significant ($p>0.05$), *$p<0.05$, **$p=0.01$-0.001, and
1272 ****$p<0.0001$.

1273 **Figure 3 – Supplement 1. Aberrant Pickpocket channel activity disrupts dendrite**
1274 **morphogenesis.**
1275
1276 Images of ddaC neurons in live 3rd instar larvae (120 h AEL). Neuron morphology was
1277 visualized with CD4::GFP (*ppk-CD4::GFP*).
1278
1279 **(A)** Representative images of control neurons and neurons overexpressing wild-type Ppk26
1280 (*UAS-Ppk26::mCherry*) or Ppk26 with the degenerin mutation [*UAS-Ppk26-*
1281 *DEG(A457V)::mCherry*]. *Ppk-Gal4* drove expression of the *UAS-Ppk26* constructs and was also
1282 included in the w^{1118} control. The overexpression of Ppk26 with the degenerin mutation resulted
1283 in variable morphologies ranging from neurons with very short primary dendrites and no axon
1284 (left) to neurons with short primary and secondary dendrites (middle) to neurons with a severely
1285 reduced dendritic arbor (right).
1286
1287 **(B)** Representative images of neurons in larvae lacking Ppk1 (Δppk1: $ppk1^{attP\text{-}KO/attP\text{-}KO}$) and, as
1288 indicated, overexpressing wild-type Ppk26 (*UAS-Ppk26::mCherry*) or Ppk26 with the degenerin
1289 mutation [*UAS-Ppk26-DEG(A457V)::mCherry*]. *Ppk-Gal4* drove expression of the *UAS-Ppk26*
1290 constructs and was also included in the Δppk1 control. In the absence of Ppk1, the
1291 overexpression of Ppk26 with the degenerin mutation resulted in the loss of ddaC neurons or
1292 ddaC neurons with a small cell body with no discernable axon or dendrites.
1293
1294 Scale bars, 100 μm and 25 μm (dashed-outline boxes).

1295 **Figure 4. Ppk1 levels are not affected by decreasing dendrite arbor size but are reduced**
1296 **when dendrite length increases.**
1297
1298 Images of ddaC neuron morphology in live 2nd instar larvae (72 h AEL). The dendritic membrane
1299 is marked by CD4::tdTomato, unless otherwise noted. Zoomed inset images show Ppk1::sfGFP
1300 in segments of dendrite in live 3rd instar larvae (120 h AEL).
1301
1302 **(A)** Representative images and quantification of control and *Rpl22-RNAi*-expressing neurons.
1303 Quantification, dendrite length: Student's unpaired t-test ($p<0.0001$); control (13 neurons, 6
1304 larvae) v. *Rpl22-RNAi* (13 neurons, 5 larvae). Dendrite length of *Rpl22-RNAi*-expressing
1305 neurons was quantified using Ppk1::sfGFP because the CD4::tdTomato signal was too dim to
1306 analyze in these mutants. Quantification, dendrite tip number: Mann-Whitney test ($p<0.0001$);
1307 control (13 neurons, 6 larvae) v. *Rpl22-RNAi* (13 neurons, 5 larvae). Quantification,
1308 Ppk1::sfGFP, dendrites: Student's unpaired t-test ($p=0.8602$); control (20 neurons, 9 larvae) v.
1309 *Rpl22-RNAi* (27 neurons, 14 larvae).
1310
1311 **(B)** Representative images and quantification of control and *EcR-DN*-expressing neurons.
1312 Quantification, dendrite length: Student's unpaired t-test ($p<0.0001$); control (15 neurons, 9
1313 larvae) v. *EcR-DN* (15 neurons, 7 larvae). Quantification, dendrite tip number: Student's
1314 unpaired t-test ($p<0.0001$); control (15 neurons, 9 larvae) v. *EcR-DN* (15 neurons, 7 larvae).
1315 Quantification, Ppk1::sfGFP, dendrites: Student's unpaired t-test ($p=0.2318$); control (24
1316 neurons, 10 larvae) v. *EcR-DN* (23 neurons, 10 larvae).
1317
1318 **(C)** Representative images and quantification of control neurons and neurons over-expressing
1319 *Rac1* (*Rac1* O/E). Quantification, dendrite length: Student's unpaired t-test ($p=0.7618$); control
1320 (15 neurons, 10 larvae) v. *Rac1* O/E (14 neurons, 5 larvae). Quantification, dendrite tip number:
1321 Student's unpaired t-test ($p<0.0001$); control (15 neurons, 10 larvae) v. *Rac1* O/E (14 neurons, 5
1322 larvae). Quantification, Ppk1::sfGFP, dendrites: Student's unpaired t-test ($p=0.0791$); control (20
1323 neurons, 9 larvae) v. *Rac1* O/E (20 neurons, 9 larvae).
1324
1325 **(D)** Representative images and quantification of control neurons and neurons over-expressing
1326 *PI3K* (*PI3K* O/E). Quantification, dendrite length: Student's unpaired t-test ($p=0.0001$); control
1327 (12 neurons, 5 larvae) v. *PI3K* O/E (12 neurons, 6 larvae). Quantification, dendrite tip number:
1328 Student's unpaired t-test ($p=0.0002$); control (12 neurons, 5 larvae) v. *PI3K* O/E (12 neurons, 6

larvae). Quantification, Ppk1::sfGFP, dendrites: Student's unpaired t-test ($p<0.0001$); control (26 neurons, 14 larvae) v. *PI3K* O/E (22 neurons, 13 larvae).

Control genotype: w^{1118}; *ppk-Gal4*. Experimental genotypes: *ppk-Gal4* was used to express the indicated construct. *CD4::tdTomato* and *Ppk1::sfGFP* included as indicated. Experiments to analyze the effects of *Rpl22-RNAi* and *Rac1 over-expression* were run together; the controls for these experiments are the same. In the graphs, each data point represents a neuron, and data are plotted as mean ± SEM. n.s.=not significant ($p>0.05$), ***$p=0.001$-0.0001, and ****$p<0.0001$. AU: arbitrary units. Scale bars, 50 μm.

1338 **Figure 5. Ppk1 persists in dendrites when dynein-mediated transport is disrupted, and**
1339 **dynein plays a role transporting Ppk1 away from Golgi.**
1340
1341 Images of ddaC neurons in live 3rd instar larvae. Dashed-outline boxes: zoomed-in views of
1342 dendrite branches, cell bodies, and axons.
1343
1344 **(A)** Representative images and quantification of Ppk1::sfGFP in control (21 neurons, 11 larvae)
1345 and *Dlic-RNAi*-expressing neurons (21 neurons, 11 larvae). Quantification, dendrites: Student's
1346 unpaired t-test ($p=0.7756$). Quantification, axons: Mann-Whitney test ($p<0.0001$). Scale bars, 50
1347 µm and 5 µm (dashed-outline boxes).
1348
1349 **(B)** Representative images and quantification of Ppk1::sfGFP in control neurons and neurons
1350 over-expressing *dmn* (O/E *dmn*). Quantification, dendrites, 72 h AEL: Mann Whitney
1351 ($p=0.1417$); control (16 neurons, 6 larvae) v. O/E *dmn* (14 neurons, 6 larvae). Quantification,
1352 dendrites, 120 h AEL: Student's unpaired t-test ($p<0.0001$); control (20 neurons, 12 larvae) v.
1353 O/E *dmn* (24 neurons, 14 larvae). Quantification, axons, 120 h AEL: Mann-Whitney test
1354 ($p<0.0001$); control (20 neurons, 12 larvae) v. O/E *dmn* (23 neurons, 14 larvae). Scale bars, 50
1355 µm and 5 µm (dashed-outline boxes).
1356
1357 **(C)** Representative images of Ppk1::sfGFP and GALNT2::TagRFP in control and *Dlic-RNAi*-
1358 expressing neurons. In *Dlic-RNAi*-expressing neurons, Ppk1::sfGFP (green arrowheads)
1359 accumulates in Golgi in the cell body and Golgi outposts, marked by GALNT2::TagRFP
1360 (magenta arrowheads). Scale bars, 10 µm (solid-outline boxes; dashed-outline boxes, cell body)
1361 and 5 µm (dashed-outline boxes, dendrites).
1362
1363 **(D)** Representative images of Ppk1::sfGFP and GALNT2::TagRFP in the axons of control and
1364 *Dlic-RNAi*-expressing neurons. Zoomed-in images of an axon of a *Dlic-RNAi*-expressing neuron
1365 shows that the Ppk1::sfGFP puncta (green arrowheads) do not colocalize with ectopic Golgi
1366 marked by GALNT2::TagRFP (magenta arrowheads). Scale bars, 10 µm and 5 µm (dashed-
1367 outline boxes).
1368
1369 **(E)** Representative images of GALNT2::TagRFP and Ppk1::sfGFP in the axons of control and
1370 Lva-DN-expressing neurons. In Lva-DN, GALNT2::TagRFP mislocalizes to axons (blue
1371 arrowheads) and axonal Ppk1::sfGFP levels increase. Quantification, Ppk1::sfGFP, axons:

1372 Student's unpaired t-test ($p<0.0001$); control (17 neurons, 6 larvae) v. Lva-DN (16 neurons, 7
1373 larvae). Scale bar, 10 µm.
1374
1375 Control genotypes: *w*^{1118}; *ppk-Gal4*. Experimental genotypes: *w*^{1118}; *ppk-Gal4 UAS-Dlic-RNAi*
1376 *UAS-Dicer* (A, C, D), *w*^{1118}; *ppk-Gal4 UAS-dmn* (B), *w*^{1118}; *ppk-Gal4 UAS-Lva-DN* (E). *UAS-*
1377 *GALNT2::TagRFP* and *Ppk1::sfGFP* included as indicated (A-E). In the graphs, each data point
1378 represents a neuron and data are plotted as mean ± SEM. n.s.=not significant ($p>0.05$) and
1379 ****$p<0.0001$. AU: arbitrary units.

1380 **Figure 6. Disrupting secretory pathway function reduces both dendrite growth and**
1381 **membrane-expressed Ppk1.**
1382
1383 Images of ddaC neurons in live 3rd instar larvae. Dashed-outline boxes: zoomed-in views of
1384 dendrite branches.
1385
1386 **(A)** Representative images and quantification of neuron morphology in control (12 neurons, 6
1387 larvae) and *Sec23-gRNA*-expressing (12 neurons, 5 larvae) neurons. The neuronal membrane
1388 is marked by CD4::tdTomato. Quantification, dendrite length: Mann-Whitney test ($p<0.0001$).
1389 Quantification, dendrite tip number: Student's unpaired t-test ($p<0.0001$). Scale bar, 100 μm.
1390
1391 **(B)** Representative images and quantification of Ppk1::GFP(11x3)^{EC}::mCherry$^{C\text{-}term}$ in control
1392 and *Sec23-gRNA*-expressing neurons. Quantification, reconstituted GFP, dendrites: Student's
1393 unpaired t-test ($p<0.0001$); control (18 neurons, 8 larvae) v. *Sec23-gRNA* (12 neurons, 8
1394 larvae). Quantification, mCherry, dendrites: Student's unpaired t-test ($p=0.0039$); control (18
1395 neurons, 8 larvae) v. *Sec23-gRNA* (14 neurons, 8 larvae). Quantification, mCherry, axons:
1396 Student's unpaired t-test ($p=0.0002$); control (17 neurons, 8 larvae) v. *Sec23-gRNA* (13
1397 neurons, 8 larvae). Scale bars, 50 μm and 10 μm (dashed-outline boxes).
1398
1399 **(C)** Representative images and quantification of Ppk1::sfGFP in control and *Sec23-gRNA*-
1400 expressing neurons. Quantification, dendrites: Student's unpaired t-test ($p=0.1414$); control (26
1401 neurons, 15 larvae) v. *Sec23-gRNA* (20 neurons, 11 larvae). Quantification, axons: Student's
1402 unpaired t-test ($p<0.0001$); control (26 neurons, 15 larvae) v. *Sec23-gRNA* (16 neurons, 10
1403 larvae). Scale bars, 50 μm and 10 μm (dashed-outline boxes).
1404
1405 Control genotypes: *w^{1118}*; *ppk-Cas9*. Experimental genotype: *w^{1118}*; *ppk-Cas9 U6-Sec23-gRNA*.
1406 *ppk-CD4::tdTomato*, *Ppk1::GFP(11x3)^{EC}::mCherry$^{C\text{-}term}$*, and *Ppk1::sfGFP* included as indicated
1407 (A-C). In the graphs, each data point represents a neuron, and data are plotted as mean ± SEM.
1408 n.s.=not significant ($p>0.05$), **$p=0.01$-0.001, ***$p=0.001$-0.0001, and ****$p<0.0001$. AU:
1409 arbitrary units.

1410 **Figure 7. Normal dendritic levels of Ppk1 rely on Rab11.**

1411

1412 Images of ddaC neurons in 3rd instar larvae, fixed (A, D) or live (B, C, E). Dashed-outline boxes:
1413 zoomed-in images of cell bodies.

1414

1415 **(A)** Representative images and quantification of membrane-expressed Ppk1, recognized by
1416 anti-Ppk1 antibodies, in control (18 neurons, 6 larvae) and *Rab11-RNAi*^{108382}-expressing
1417 neurons (18 neurons, 6 larvae).

1418

1419 **(B)** Representative images and quantification of Ppk1::sfGFP in the dendrites and cell bodies of
1420 control (23 neurons, 18 larvae) and *Rab11-RNAi*^{108382}-expressing neurons (24 neurons, 12
1421 larvae).

1422

1423 **(C)** Representative images and quantification of Ppk1::mCherry in the dendrites of control (20
1424 neurons, 10 larvae) and *Rab11-RNAi*^{108382}-expressing neurons (23 neurons, 11 larvae).

1425

1426 **(D)** Representative image and quantification of membrane-expressed Ppk1, recognized by anti-
1427 Ppk1 antibodies, in control (19 neurons, 6 larvae) and *Rab11-DN*-expressing neurons (18
1428 neurons, 6 larvae). In ddaC neurons expressing Rab11-DN, Ppk1 immunostaining in the cell
1429 body was frequently observed (blue arrowhead).

1430

1431 **(E)** Representative images and quantification of Ppk1::mCherry in control (28 neurons, 12
1432 larvae) and *Rab11-DN*-expressing neurons (28 neurons, 14 larvae).

1433

1434 Control genotype: *w*^{1118}; *ppk-Gal4*. Experimental genotypes: *w*^{1118}; *ppk-Gal4 UAS-Rab11-*
1435 *RNAi*^{108382} (A-C) and *w*^{1118}; *ppk-Gal4 UAS-Rab11-DN::GFP* (D, E). *Ppk1::sfGFP* or
1436 *Ppk1::mCherry* included as indicated (A-E). -Tx: no Triton X-100 (non-permeabilizing
1437 conditions). In the graphs, each data point represents a neuron, and data are plotted as mean ±
1438 SEM. Quantification: Student's unpaired t-test. ****$p<0.0001$. AU: arbitrary units. Scale bars, 50
1439 µm and 10 µm (dashed-outline boxes).

1440 **Figure 7 – Supplement 1. Disrupting Rab11 levels or activity causes a reduction in**
1441 **dendrite arbor growth.**
1442
1443 Representative images of ddaC neurons in 72 h AEL larvae and quantification of dendrite length
1444 and dendrite tip number in control neurons (w^{1118}; 14 neurons, 6 larvae) and neurons over-
1445 expressing *Rab11-RNAi*^{108382} (16 neurons, 7 larvae) or *Rab11-DN* (15 neurons, 7 larvae).
1446 Quantification, dendrite length: One-way ANOVA with post-hoc Tukey; w^{1118} v. *Rab11-*
1447 *RNAi*^{108382} ($p<0.0001$), w^{1118} v. *Rab11-DN* ($p<0.0001$), *Rab11-RNAi*^{108382} v. *Rab11-DN*
1448 ($p<0.0001$). Quantification, dendrite tips: One-way ANOVA with post-hoc Tukey: w^{1118} v. *Rab11-*
1449 *RNAi*^{108382} ($p<0.0001$), w^{1118} v. *Rab11-DN* ($p<0.0001$), *Rab11-RNAi*^{108382} v. *Rab11-DN*
1450 ($p<0.0001$). In the graphs, each data point represents a neuron, and data are plotted as mean ±
1451 SEM. The expression of *UAS-Rab11-RNAi*^{108382} and *UAS-Rab11-DN* was driven by *ppk-Gal4*,
1452 and *ppk-Gal4* was included in the w^{1118} control. Scale bar, 100 μm.

1453 **Figure 8. Ppk1::mCherry puncta colocalize with Rab5::GFP, but dendritic levels of Ppk1**
1454 **do not depend on Rab5 function.**
1455
1456 Images of ddaC neurons in 3rd instar larvae, live (A, C) or fixed (B). Dashed-outline boxes:
1457 zoomed-in views of dendrite branch and cell bodies.
1458
1459 **(A)** Representative images of Ppk1::mCherry with Rab5::GFP. Arrowheads: Colocalized signal.
1460 Zoomed-in view of Ppk1::mCherry and Rab5::GFP in a dendrite branch. Line trace is through
1461 the punctum highlighted by the arrowhead. Zoomed-in view of Ppk1::mCherry and Rab5::GFP
1462 in the cell body and proximal dendrites.
1463
1464 **(B)** Representative images and quantification of membrane-expressed Ppk1, recognized by
1465 anti-Ppk1 antibodies, in control neurons (14 neurons, 6 larvae) and neurons over-expressing
1466 wild-type *Rab5* (Rab5-WT; 19 neurons, 6 larvae) or *Rab5-DN* (16 neurons, 6 larvae).
1467 Quantification: one-way ANOVA with post-hoc Tukey; control v. *Rab5-WT* (p=0.1323), control v.
1468 *Rab5-DN* (p=0.1562), and *Rab5-WT* v. *Rab5-DN* (p=0.9999).
1469
1470 **(C)** Representative images and quantification of Ppk1::mCherry in control (20 neurons, 10
1471 larvae) and *Rab5-DN*-expressing neurons (20 neurons, 10 larvae). Quantification,
1472 Ppk1::mCherry levels, dendrite: Student's t-test (p=0.1782). Quantification, Ppk1::mCherry
1473 puncta number: Mann-Whitney test (p<0.0001). Ppk1::mCherry puncta were quantified in
1474 dendrites within 70 μm of the cell body.
1475
1476 Control genotype: w^{1118}; *ppk-Gal4*. Experimental genotype: w^{1118}; *ppk-Gal4 UAS-Rab5-DN::YFP*
1477 (B, C). *UAS-Rab5::GFP*, *UAS-Rab5::YFP* (Rab5-WT OE), and *Ppk1::mCherry* included as
1478 indicated (A-C). -Tx: no Triton X-100 (non-permeabilizing conditions). In the graphs, each data
1479 point represents a neuron, and data are plotted as mean ± SEM. n.s.=not significant (p<0.05)
1480 and ****p<0.0001. AU: arbitrary units. Scale bars, 50 μm and 10 μm (dashed-outline boxes).

1481 **Figure 8 – Supplement 1. Rab5-WT and Rab5-DN show a different pattern of distribution,**
1482 **and Rab5-DN reduces dendritic arbor morphogenesis.**
1483
1484 **(A)** Representative images of control ddaC neurons and ddaC neurons expressing Rab5-WT
1485 and Rab5-DN (*ppk-Gal4 UAS-Rab5-WT::YFP* and *ppk-Gal4 UAS-Rab5-DN::YFP*). The
1486 neuronal membrane is marked by CD4::tdTomato (*ppk-CD4::tdTomato*). Scale bar, 100 μm.
1487
1488 **(B)** Representative images showing the distribution of Rab5-WT::YFP and Rab5-DN::YFP in
1489 ddaC neurons from fixed larval fillets with zoomed-in images of the cell bodies (dashed-outline
1490 boxes). The neuronal membrane is marked by CD4::tdTomato (ppk-CD4::tdTomato). Scale bar,
1491 50 μm and 10 μm (dashed-outline box).

Figure 1

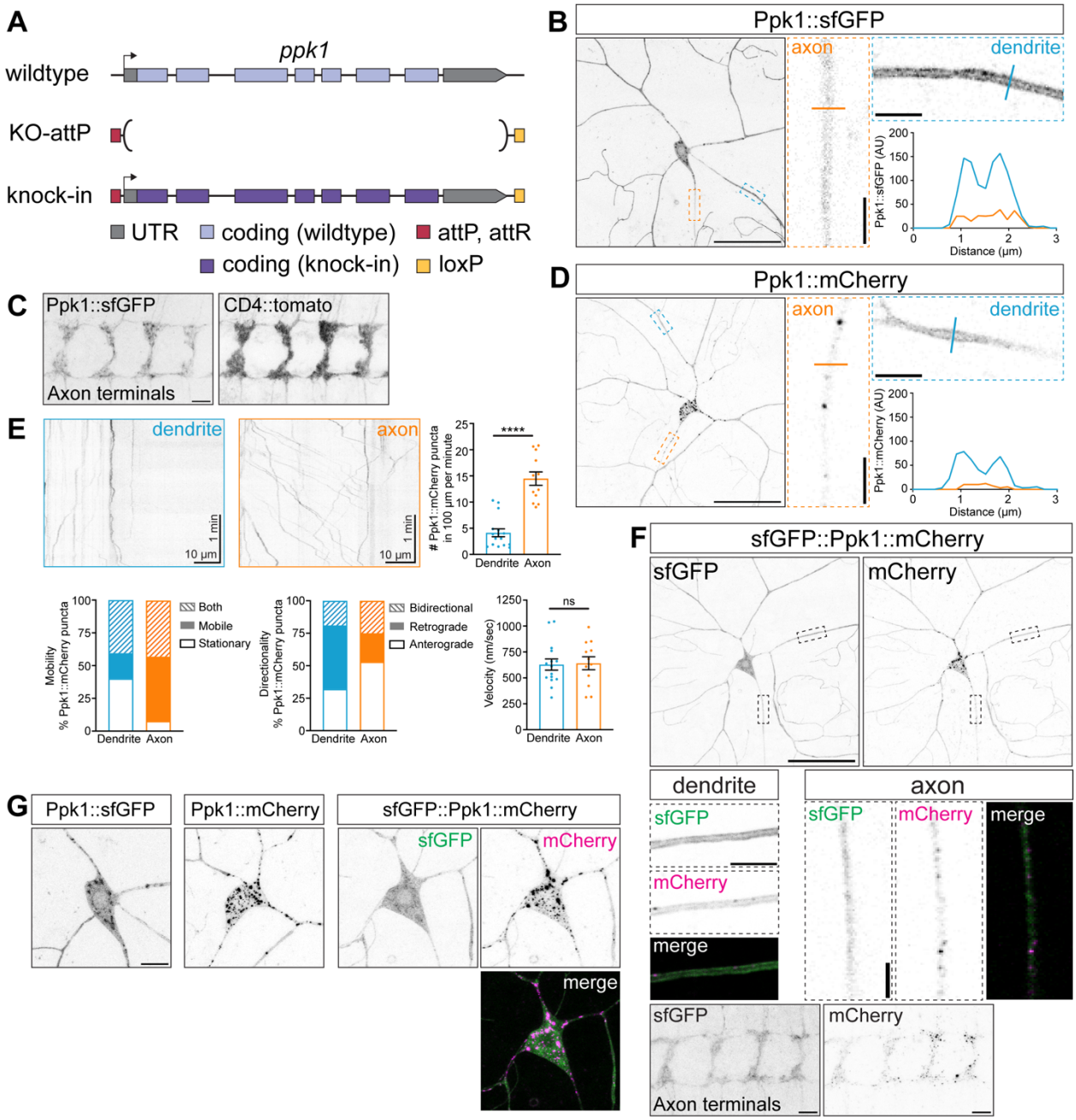
A
ppk1
wildtype
KO-attP
knock-in
UTR
coding (wildtype)
attP, attR
coding (knock-in)
loxP
B
Ppk1::sfGFP
axon
dendrite
Ppk1::sfGFP (AU)
Distance (µm)
C
Ppk1::sfGFP
CD4::tomato
Axon terminals
D
Ppk1::mCherry
axon
dendrite
Ppk1::mCherry (AU)
Distance (µm)
E
dendrite
axon
1 min
10 µm
Ppk1::mCherry puncta in 100 µm per minute
****
Dendrite
Axon
Mobility
% Ppk1::mCherry puncta
Both
Mobile
Stationary
Directionality
Bidirectional
Retrograde
Anterograde
Velocity (nm/sec)
ns
F
sfGFP::Ppk1::mCherry
sfGFP
mCherry
dendrite
axon
merge
Axon terminals
G
Ppk1::sfGFP
Ppk1::mCherry
sfGFP::Ppk1::mCherry
sfGFP
mCherry
merge

Figure 1 – Supplement 1

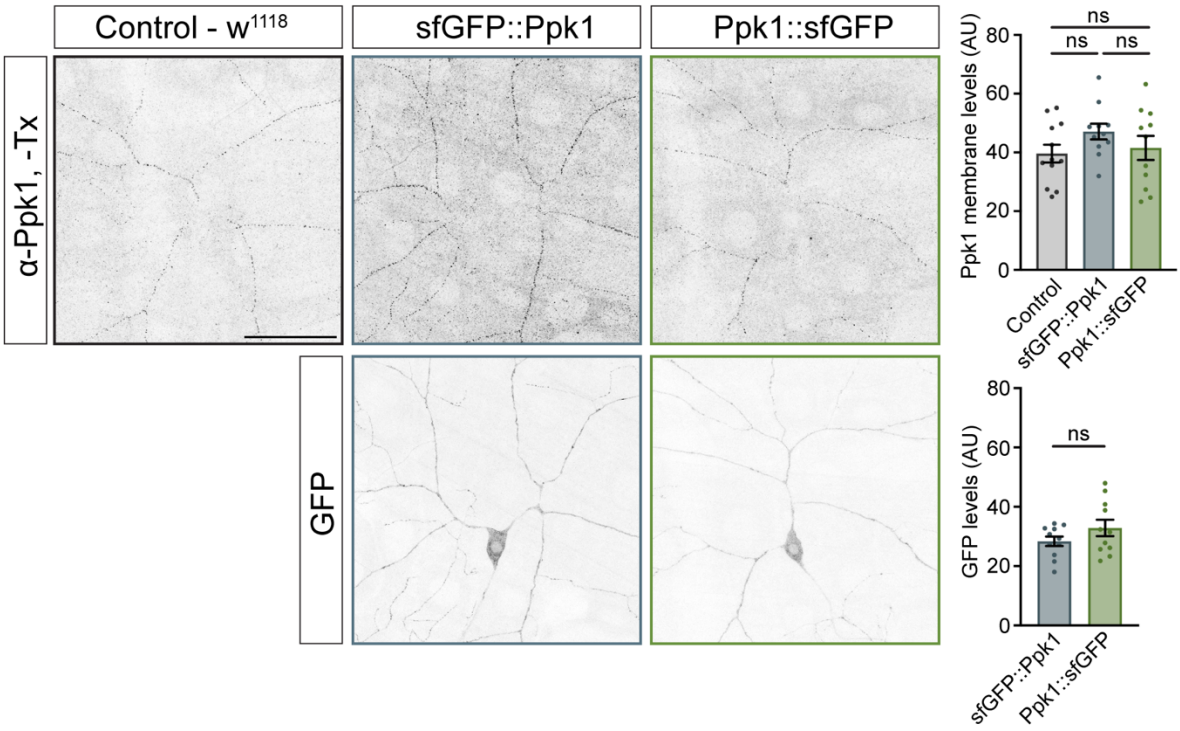

Figure 2

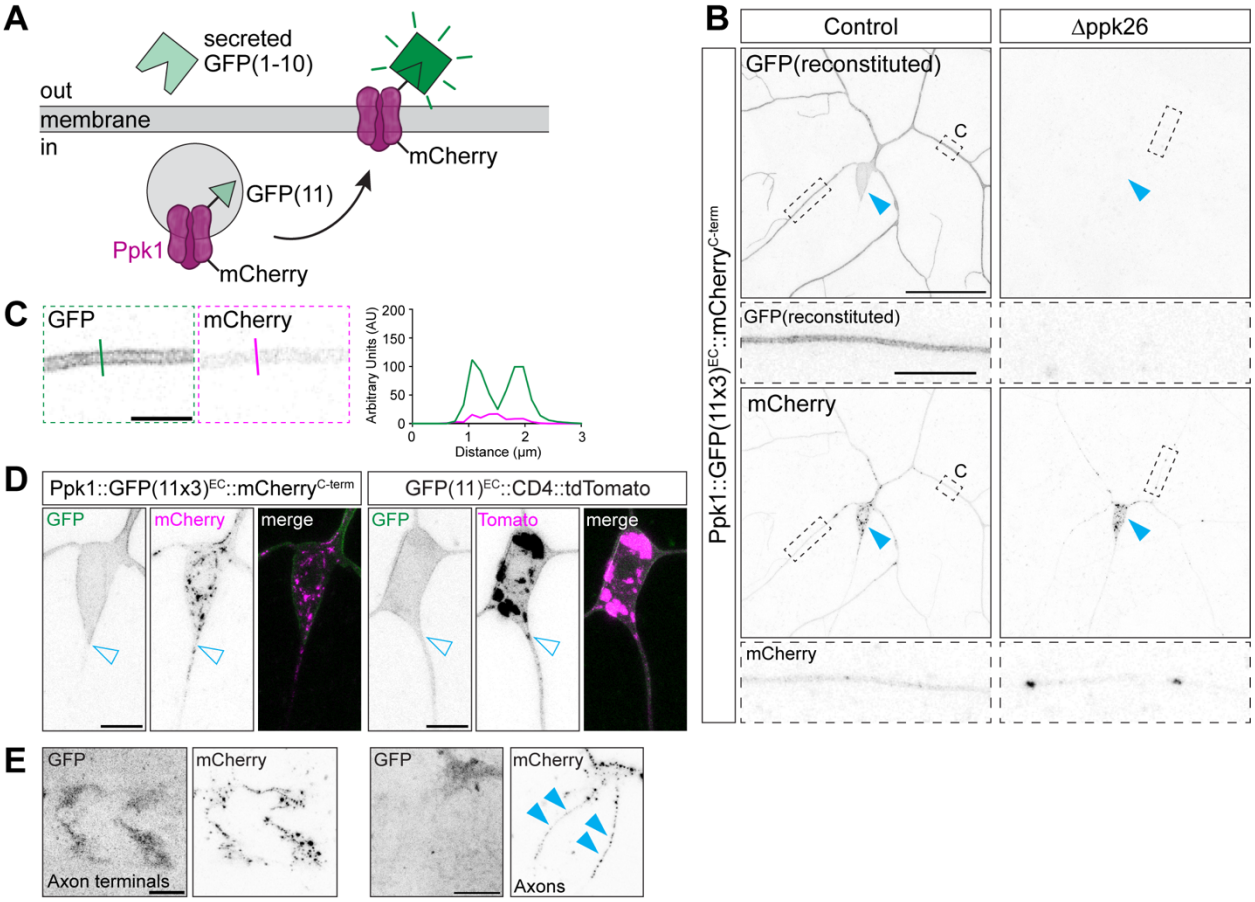
A
secreted
GFP(1-10)
out
membrane
in
mCherry
GFP(11)
Ppk1
mCherry
B
Control
Δppk26
Ppk1::GFP(11x3)EC::mCherryC-term
GFP(reconstituted)
C
GFP(reconstituted)
mCherry
C
mCherry
C
GFP
mCherry
Arbitrary Units (AU)
200
150
100
50
0
0
1
2
3
Distance (μm)
D
Ppk1::GFP(11x3)EC::mCherryC-term
GFP(11)EC::CD4::tdTomato
GFP
mCherry
merge
GFP
Tomato
merge
E
GFP
mCherry
Axon terminals
GFP
mCherry
Axons

Figure 2 – Supplement 1

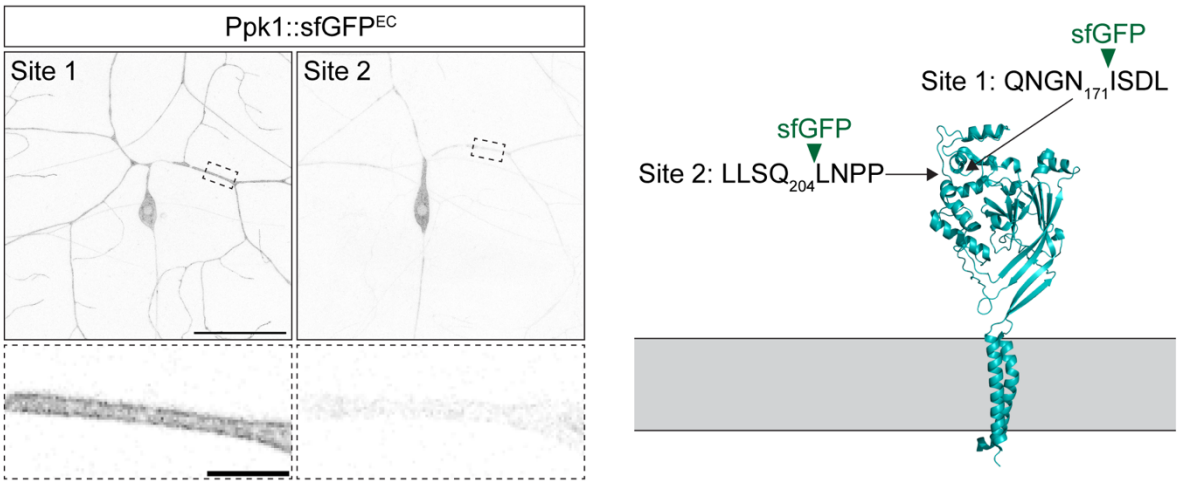

Figure 2 – Supplement 2

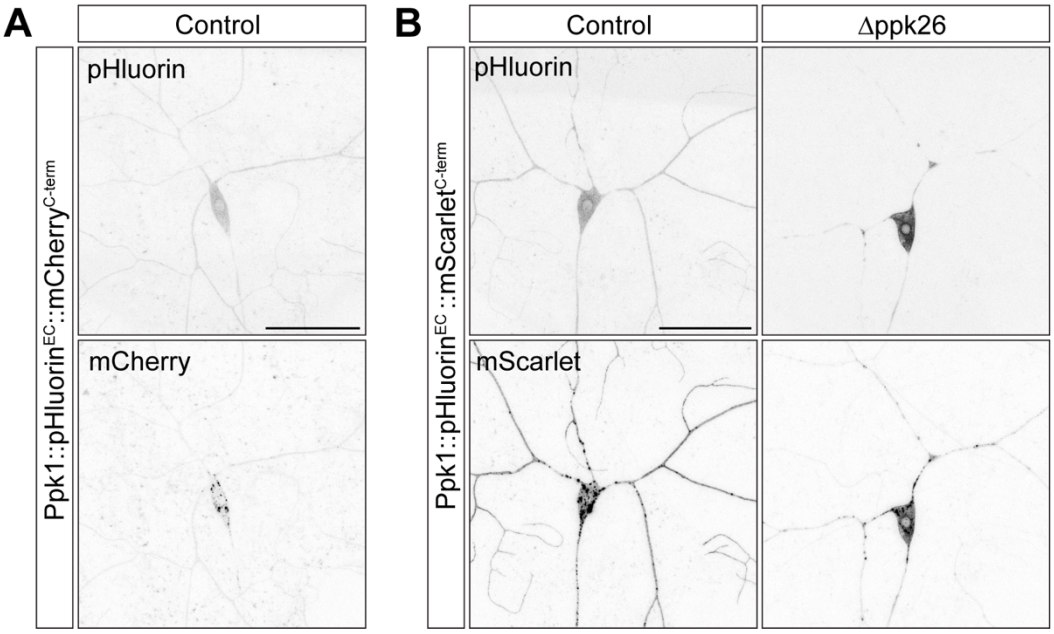

Figure 2 – Supplement 3

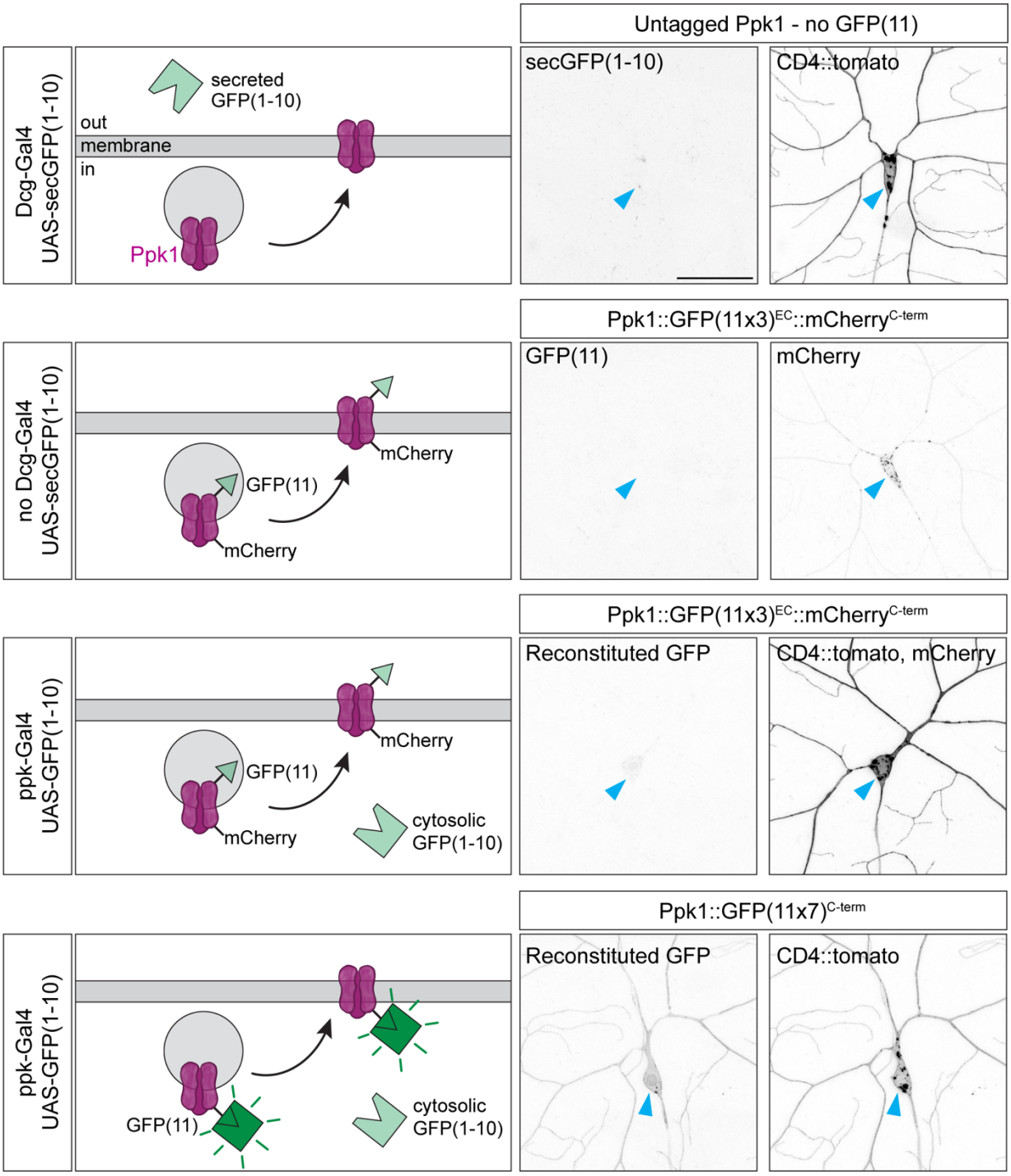

Figure 2 – Supplement 4

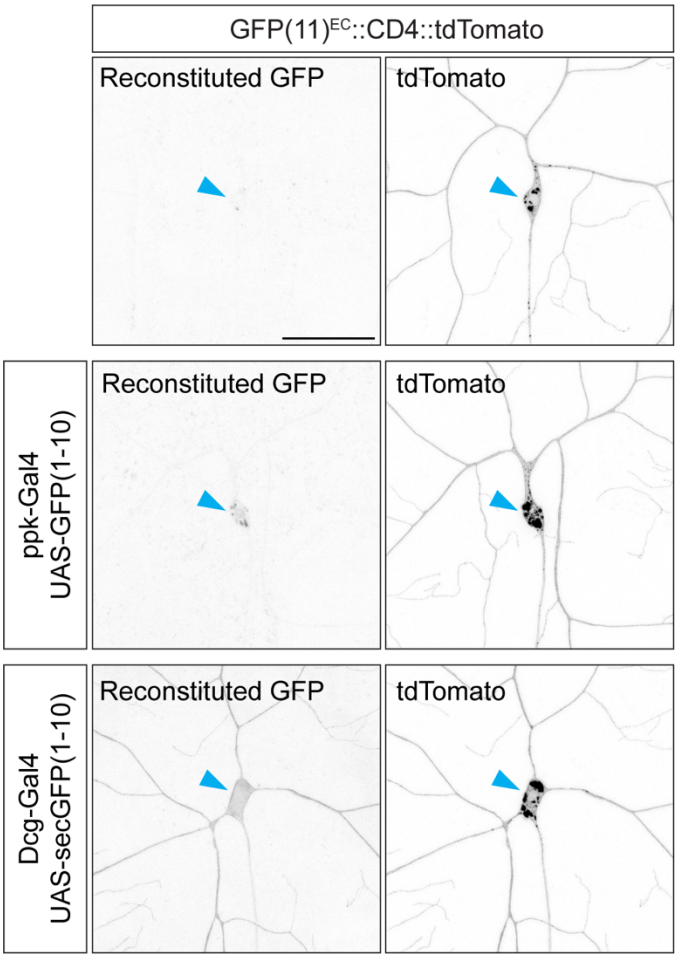

Figure 3

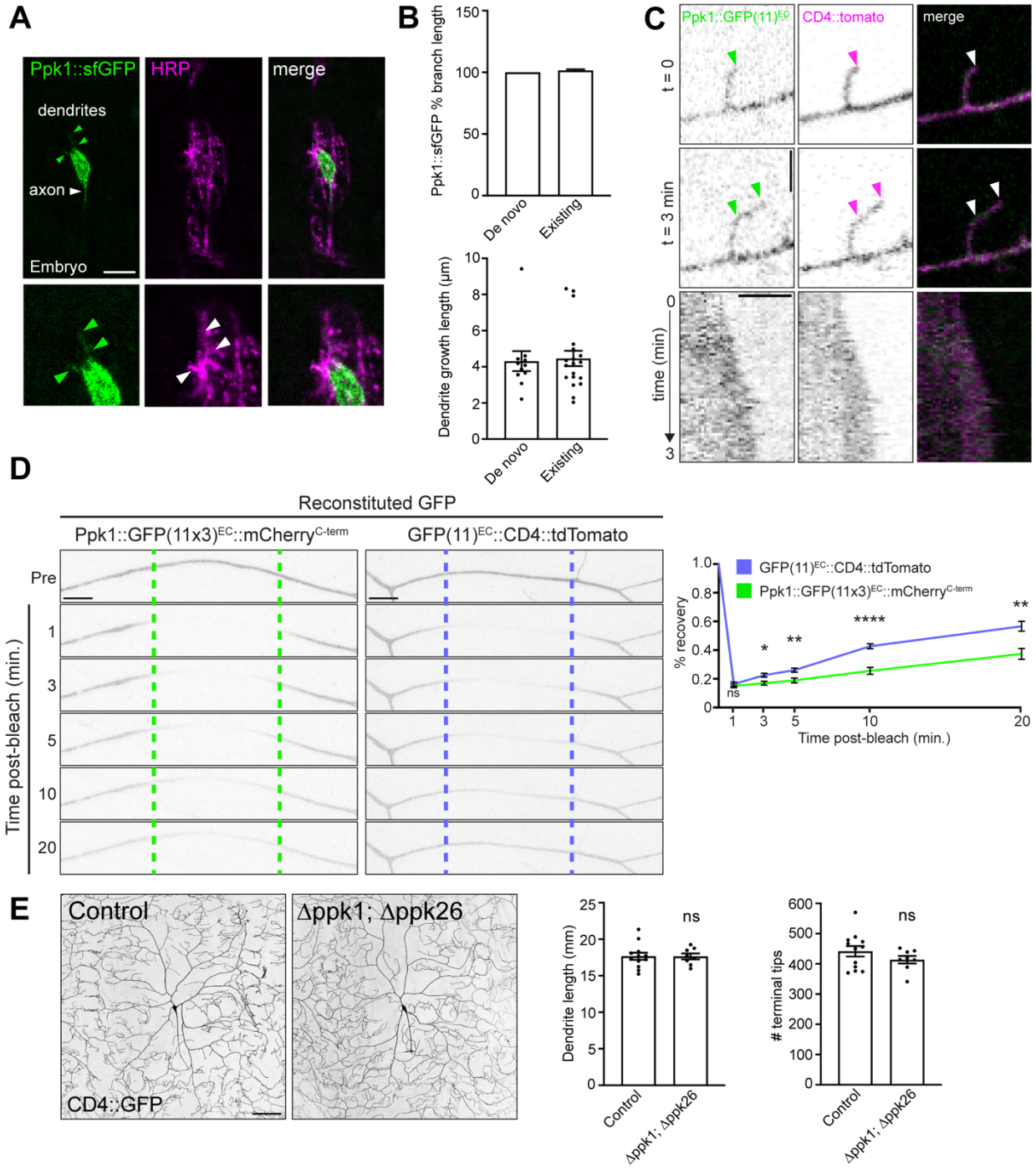
A
Ppk1::sfGFP
HRP
merge
dendrites
axon
Embryo
B
Ppk1::sfGFP % branch length
150
100
50
0
De novo
Existing
Dendrite growth length (µm)
10
8
6
4
2
0
De novo
Existing
C
Ppk1::GFP(11)EC
CD4::tomato
merge
t = 0
t = 3 min
time (min)
0
3
D
Reconstituted GFP
Ppk1::GFP(11x3)EC::mCherryC-term
GFP(11)EC::CD4::tdTomato
Pre
Time post-bleach (min.)
1
3
5
10
20
GFP(11)EC::CD4::tdTomato
Ppk1::GFP(11x3)EC::mCherryC-term
% recovery
1.0
0.8
0.6
0.4
0.2
0
ns
*
**
****
**
1
3
5
10
20
Time post-bleach (min.)
E
Control
Δppk1; Δppk26
CD4::GFP
Dendrite length (mm)
25
20
15
10
5
0
ns
Control
Δppk1; Δppk26
terminal tips
600
500
400
300
200
100
0
ns
Control
Δppk1; Δppk26

Figure 3 – Supplement 1

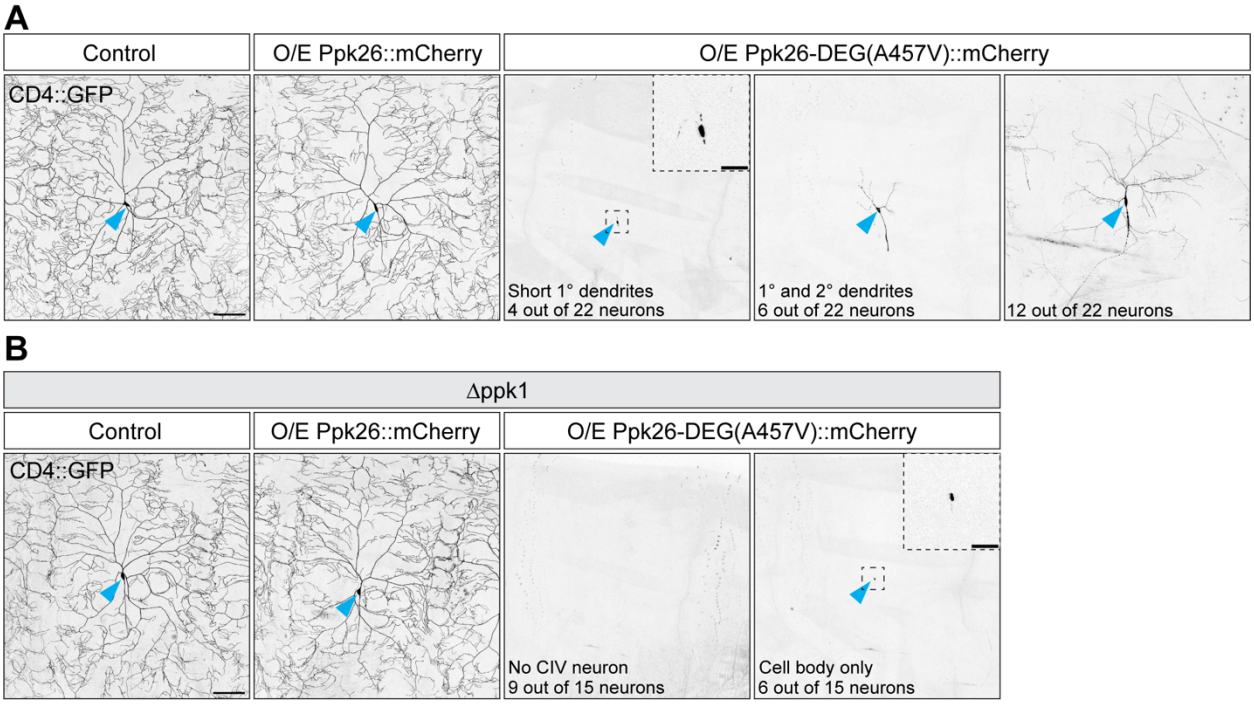

Figure 4

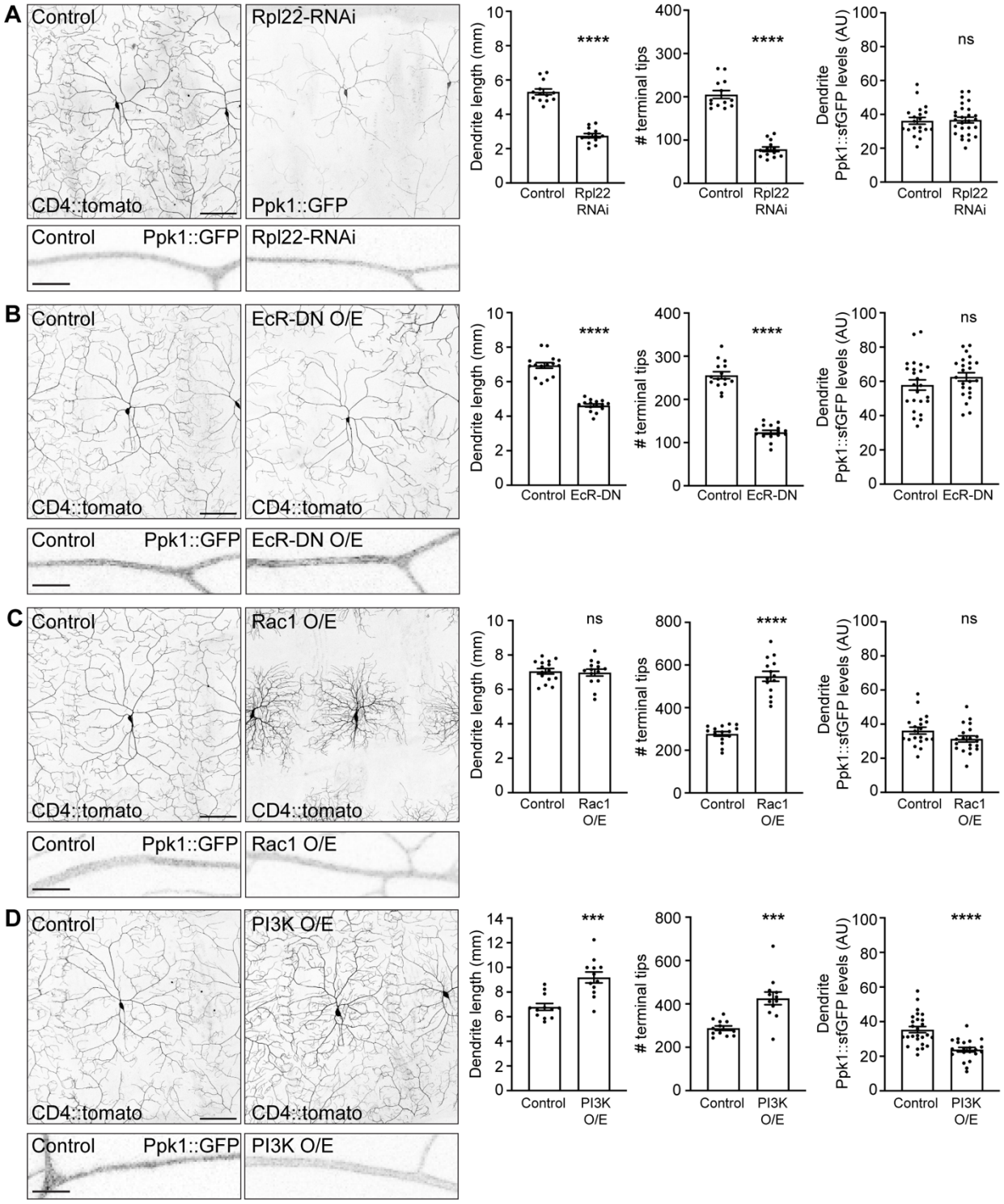
A
Control
Rpl22-RNAi
CD4::tomato
Ppk1::GFP
Control
Ppk1::GFP
Rpl22-RNAi
Dendrite length (mm)
****
Control
Rpl22 RNAi
terminal tips
****
Control
Rpl22 RNAi
Dendrite Ppk1::sfGFP levels (AU)
ns
Control
Rpl22 RNAi
B
Control
EcR-DN O/E
CD4::tomato
CD4::tomato
Control
Ppk1::GFP
EcR-DN O/E
Dendrite length (mm)
****
Control
EcR-DN
terminal tips
****
Control
EcR-DN
Dendrite Ppk1::sfGFP levels (AU)
ns
Control
EcR-DN
C
Control
Rac1 O/E
CD4::tomato
CD4::tomato
Control
Ppk1::GFP
Rac1 O/E
Dendrite length (mm)
ns
Control
Rac1 O/E
terminal tips
****
Control
Rac1 O/E
Dendrite Ppk1::sfGFP levels (AU)
ns
Control
Rac1 O/E
D
Control
PI3K O/E
CD4::tomato
CD4::tomato
Control
Ppk1::GFP
PI3K O/E
Dendrite length (mm)
***
Control
PI3K O/E
terminal tips
***
Control
PI3K O/E
Dendrite Ppk1::sfGFP levels (AU)
****
Control
PI3K O/E

Figure 5

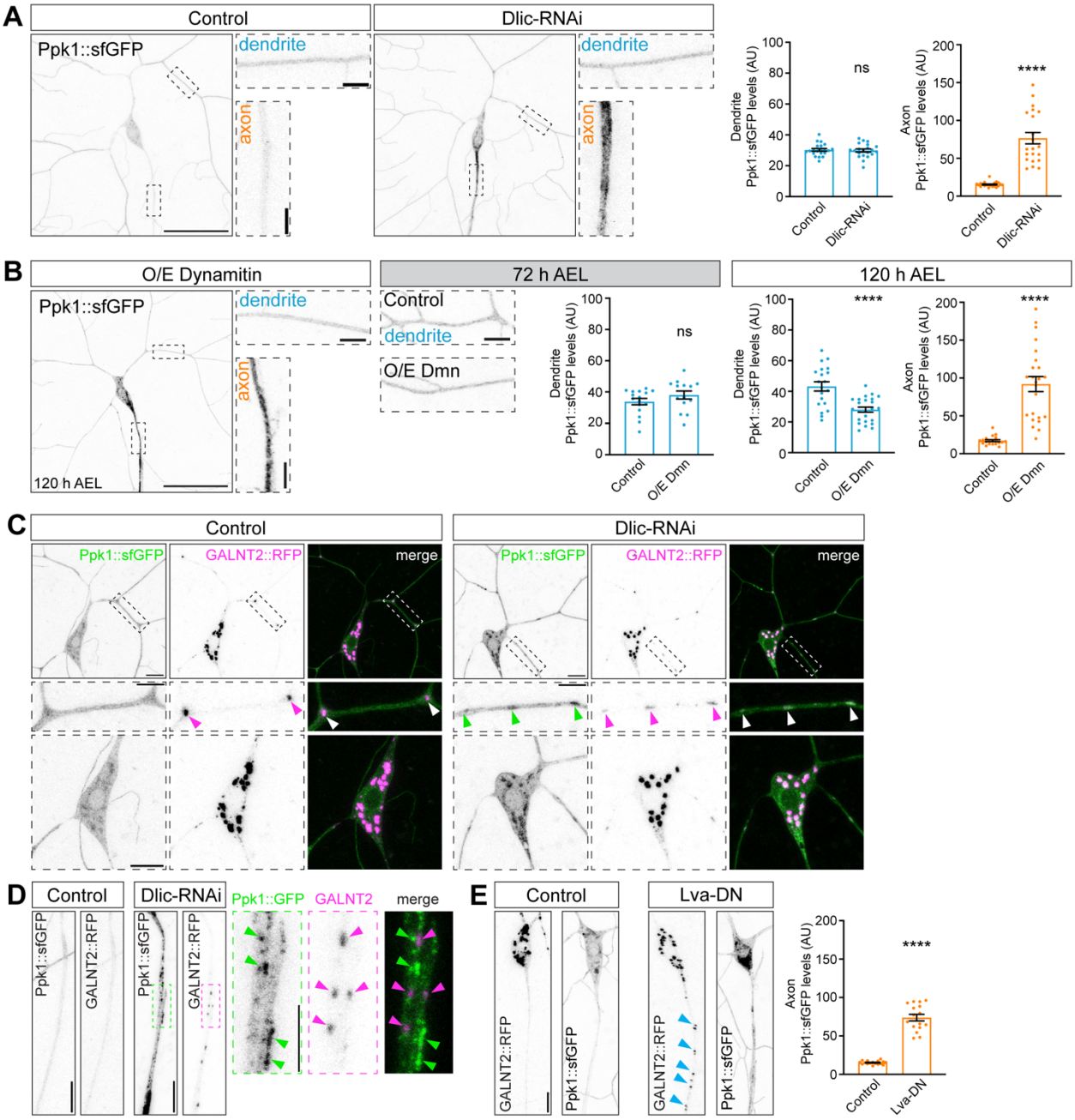
A
Control
Dlic-RNAi
Ppk1::sfGFP
dendrite
axon
Dendrite Ppk1::sfGFP levels (AU)
Axon Ppk1::sfGFP levels (AU)
ns
****
Control
Dlic-RNAi
B
O/E Dynamitin
72 h AEL
120 h AEL
O/E Dmn
120 h AEL
C
GALNT2::RFP
merge
D
Ppk1::GFP
GALNT2
E
Lva-DN

Figure 6

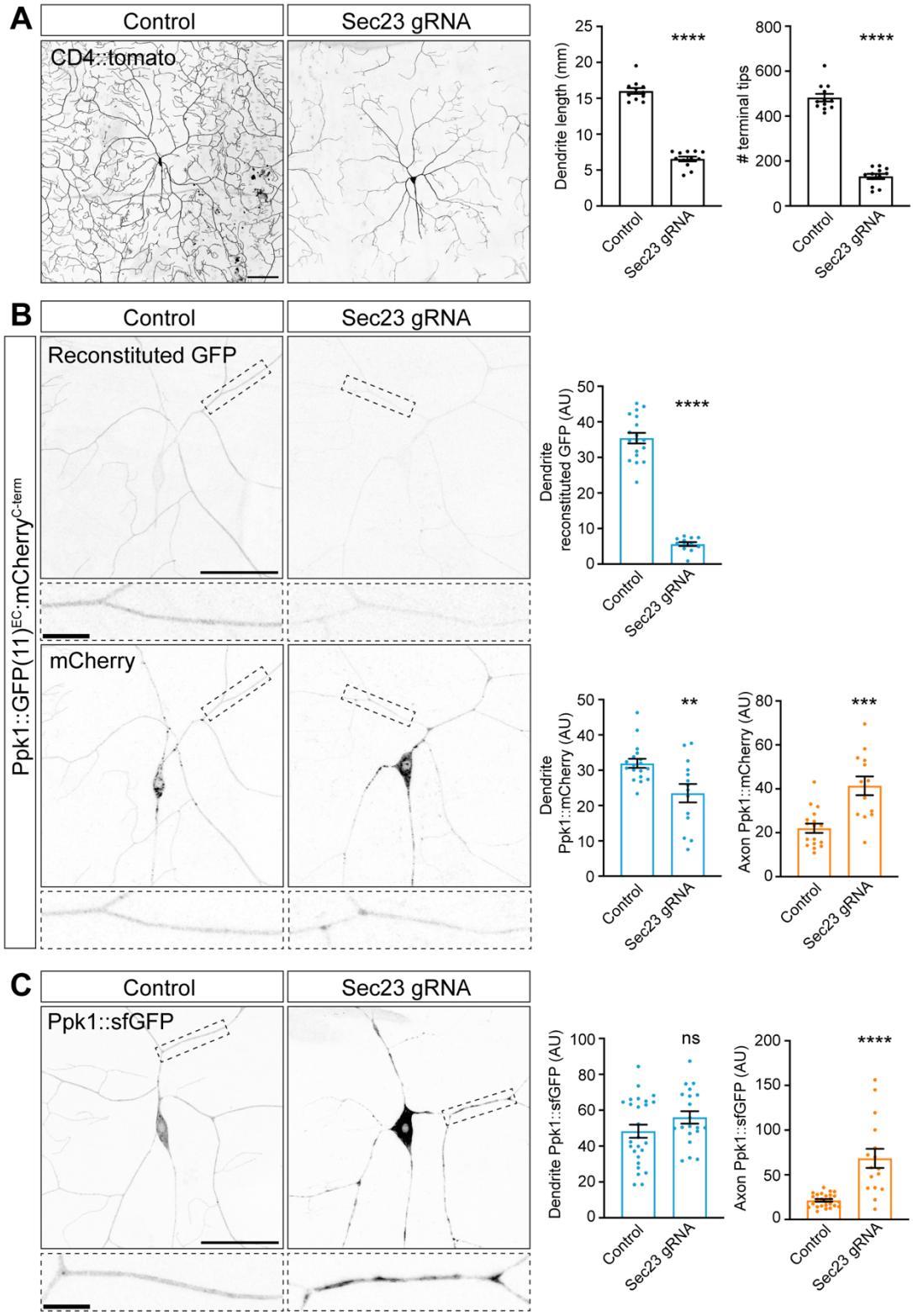
A
Control
Sec23 gRNA
CD4::tomato
Dendrite length (mm)
****
terminal tips
****
Control
Sec23 gRNA
B
Control
Sec23 gRNA
Ppk1::GFP(11)EC:mCherryC-term
Reconstituted GFP
Dendrite reconstituted GFP (AU)
****
mCherry
Dendrite Ppk1::mCherry (AU)
**
Axon Ppk1::mCherry (AU)
***
C
Control
Sec23 gRNA
Ppk1::sfGFP
Dendrite Ppk1::sfGFP (AU)
ns
Axon Ppk1::sfGFP (AU)
****

Figure 7

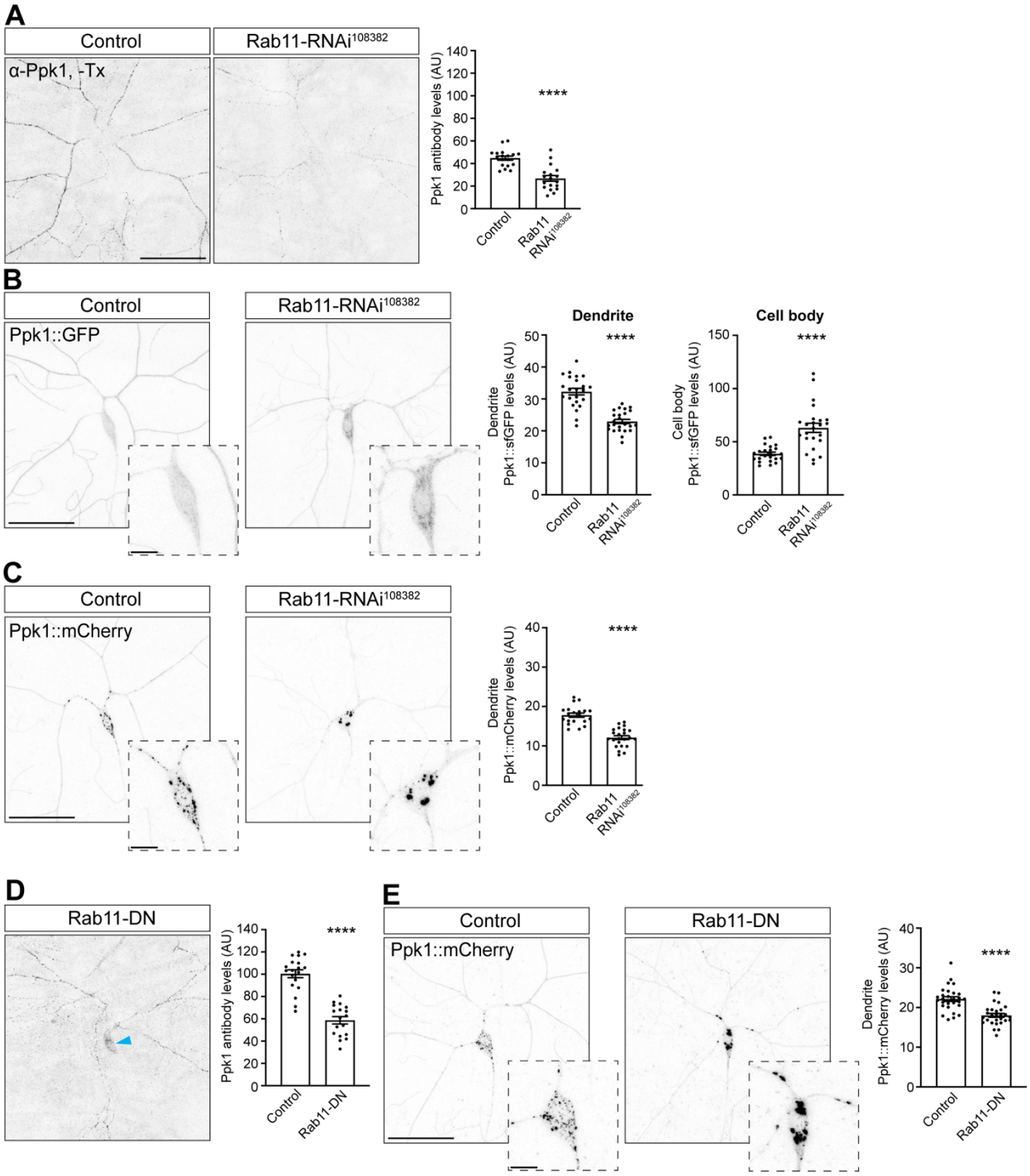
A
Control
Rab11-RNAi108382
α-Ppk1, -Tx
Ppk1 antibody levels (AU)
****
Control
Rab11 RNAi108382
B
Control
Rab11-RNAi108382
Ppk1::GFP
Dendrite
Dendrite Ppk1::sfGFP levels (AU)
Cell body
Cell body Ppk1::sfGFP levels (AU)
C
Control
Rab11-RNAi108382
Ppk1::mCherry
Dendrite Ppk1::mCherry levels (AU)
D
Rab11-DN
Ppk1 antibody levels (AU)
Control
Rab11-DN
E
Control
Rab11-DN
Ppk1::mCherry
Dendrite Ppk1::mCherry levels (AU)

Figure 7 – Supplement 1

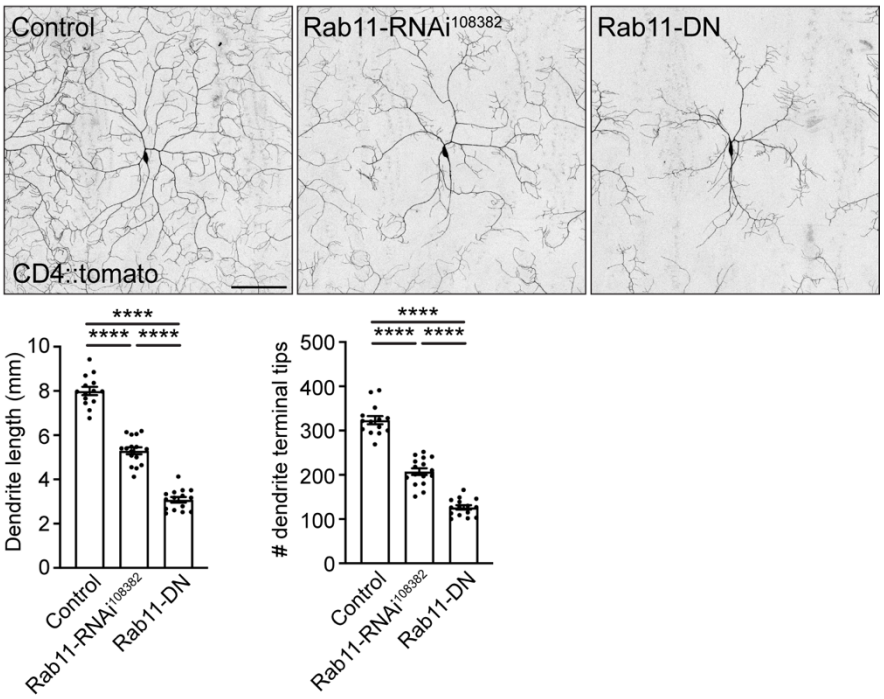

Figure 8

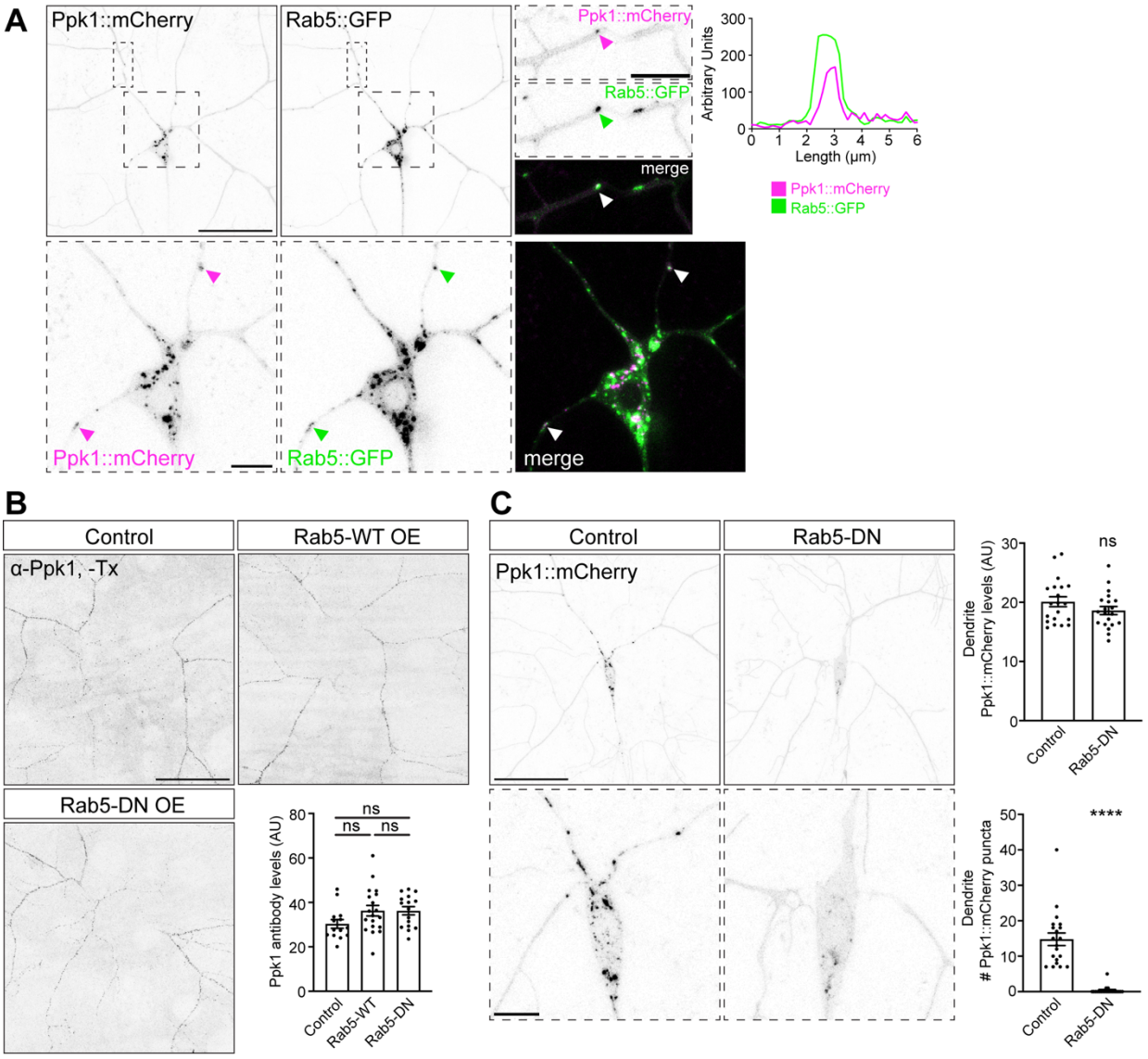
A
Ppk1::mCherry
Rab5::GFP
merge
Arbitrary Units
Length (μm)
B
Control
Rab5-WT OE
α-Ppk1, -Tx
Rab5-DN OE
Ppk1 antibody levels (AU)
ns
Control
Rab5-WT
Rab5-DN
C
Rab5-DN
Dendrite Ppk1::mCherry levels (AU)
Ppk1::mCherry puncta
****
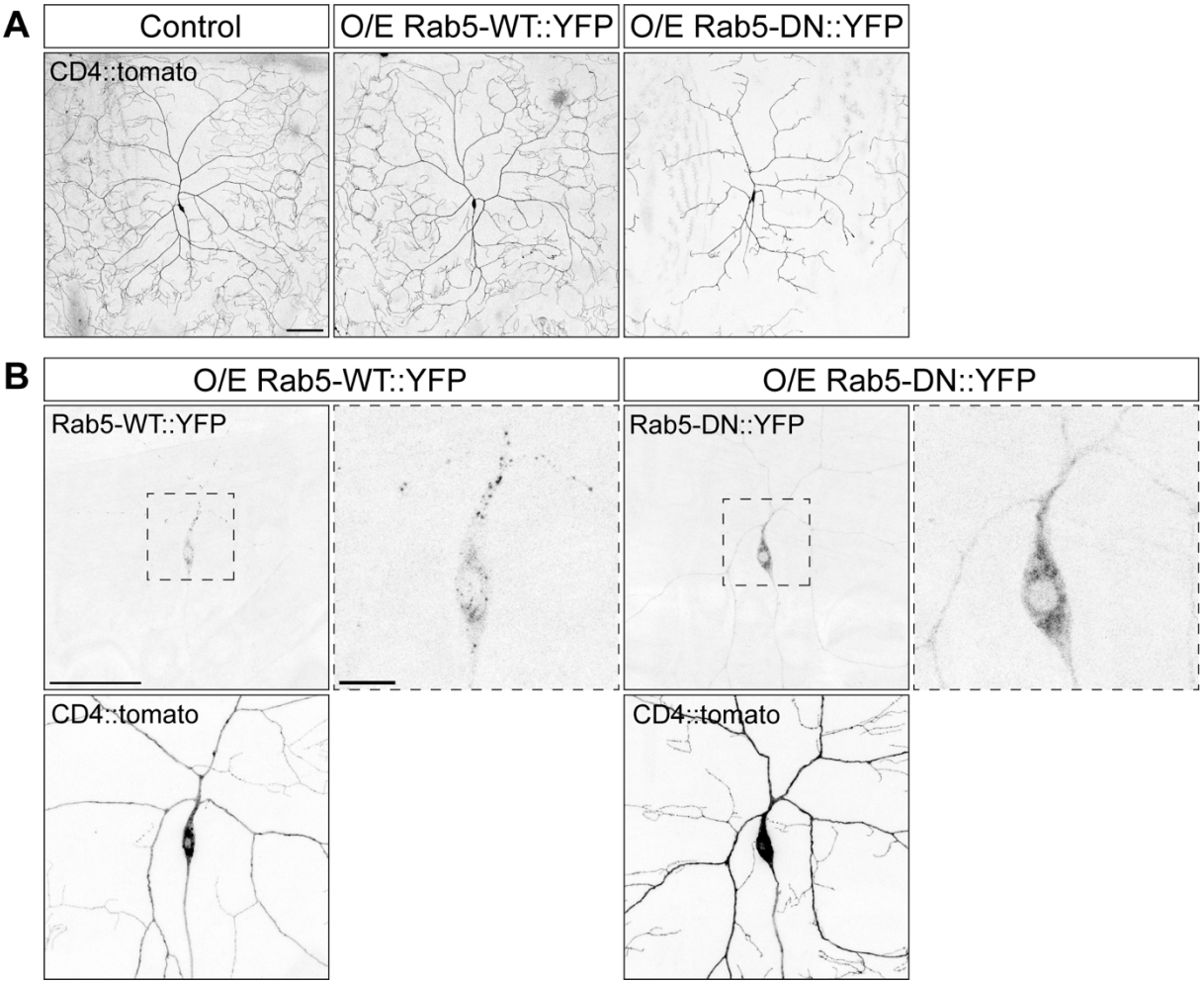
Figure 8 – Supplement 1